Supplementary Information

Quinoline-triazole half-sandwich iridium(III) complexes: Synthesis, antiplasmodial activity and preliminary transfer hydrogenation studies

Diana R. Melis [a], Chris Barnett [a], Lubbe Wiesner [b], Ebbe Nordlander [c] and Gregory S. Smith*[a]

[a] *Department of Chemistry, University of Cape Town, Rondebosch, Cape Town, South Africa. E-mail: gregory.smith@uct.ac.za*

[b] *Division of Clinical Pharmacology, Department of Medicine, University of Cape Town, Observatory 7925, Cape Town, South Africa.*

[c] *Chemical Physics, Department of Chemistry, Lund University, Box 124, SE-221 00 Lund, Sweden.*

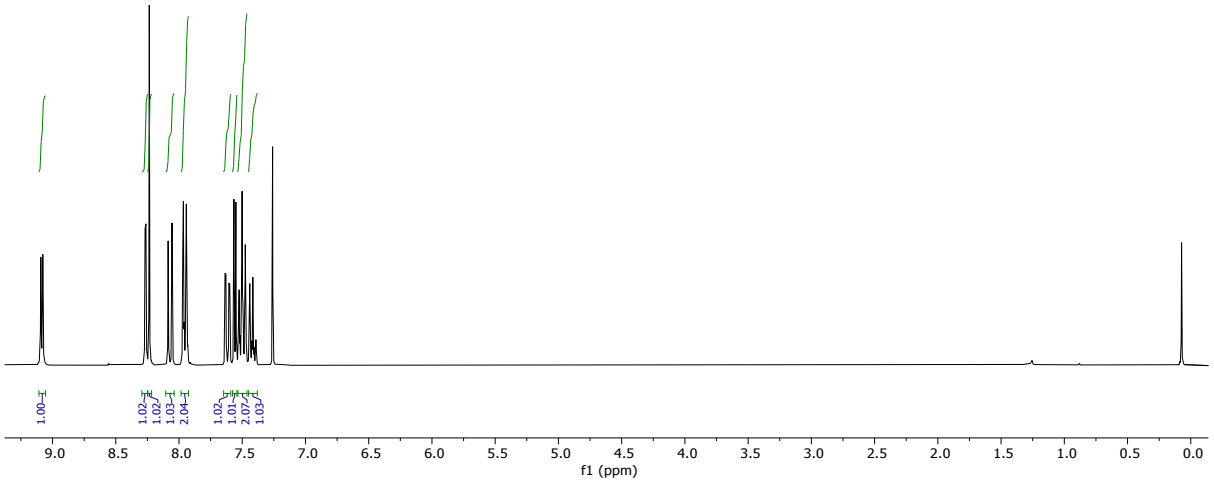
1.00
1.02
1.02
1.03
2.04
1.02
1.01
2.07
1.03
9.0 8.5 8.0 7.5 7.0 6.5 6.0 5.5 5.0 4.5 4.0 3.5 3.0 2.5 2.0 1.5 1.0 0.5 0.0
f1 (ppm)

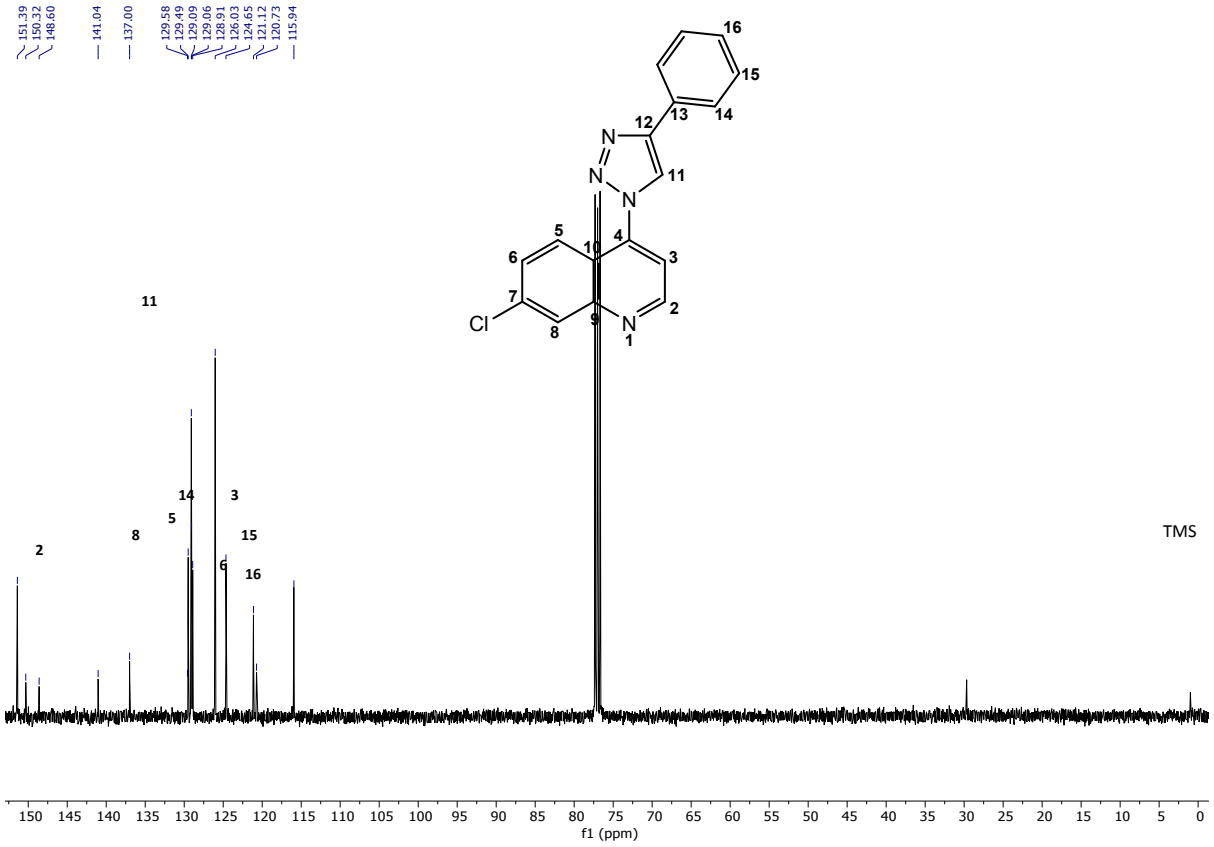
151.39
150.32
148.60
141.04
137.00
129.58
129.49
129.09
129.06
128.91
126.03
124.65
121.12
120.73
115.94
16
15
14
13
12
11
10
9
8
7
6
5
4
3
2
1
Cl
N
N
N
11
14
3
5
8
15
2
6
16
TMS
150 145 140 135 130 125 120 115 110 105 100 95 90 85 80 75 70 65 60 55 50 45 40 35 30 25 20 15 10 5 0
f1 (ppm)

Figure S1: ^{1}H and $^{13}C\{^{1}H\}$ NMR spectra of **2a** in $CDCl_3$.

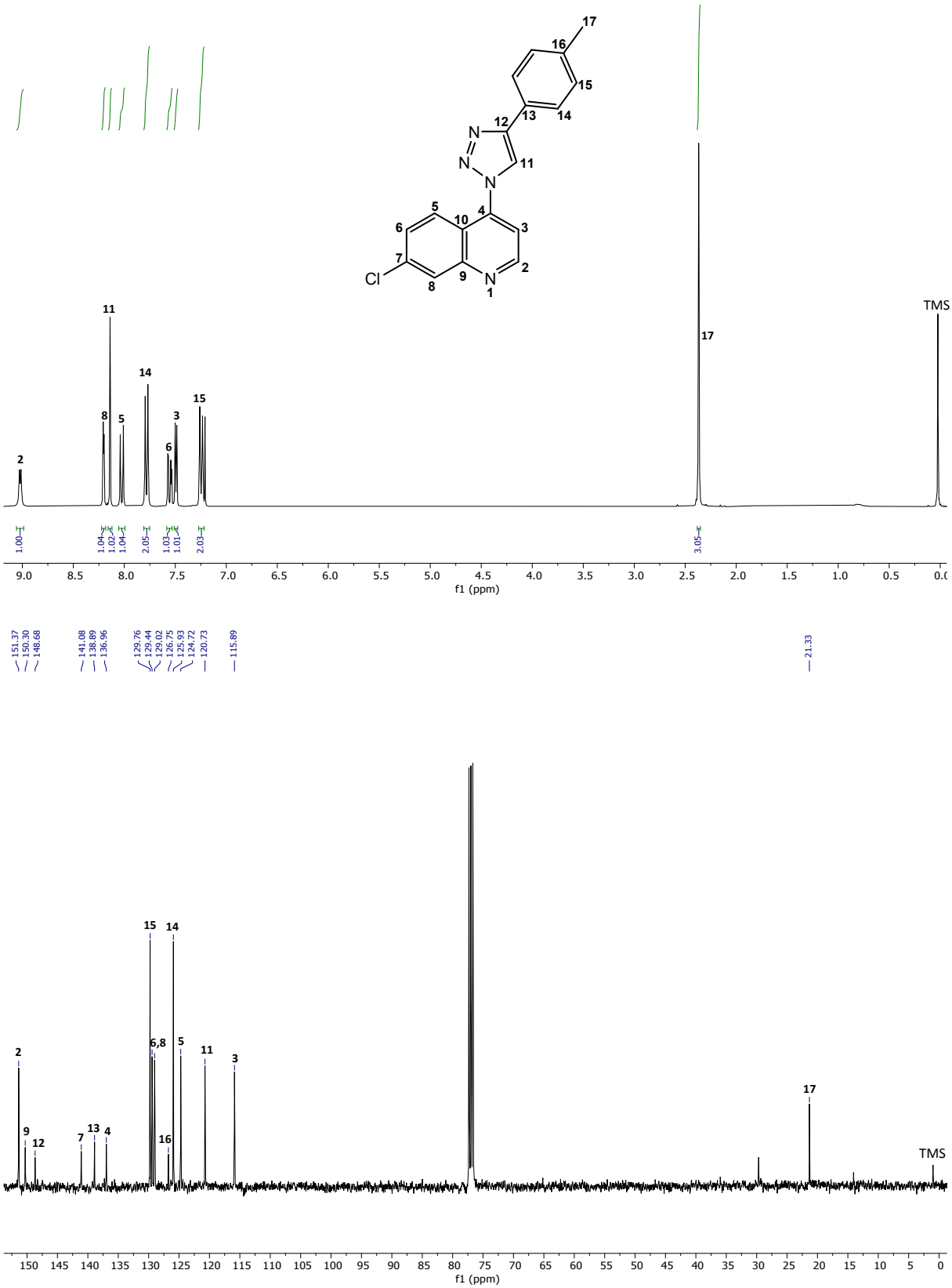

Figure S2: ^{1}H and $^{13}C\{^{1}H\}$ NMR spectra of **2b** in $CDCl_3$.

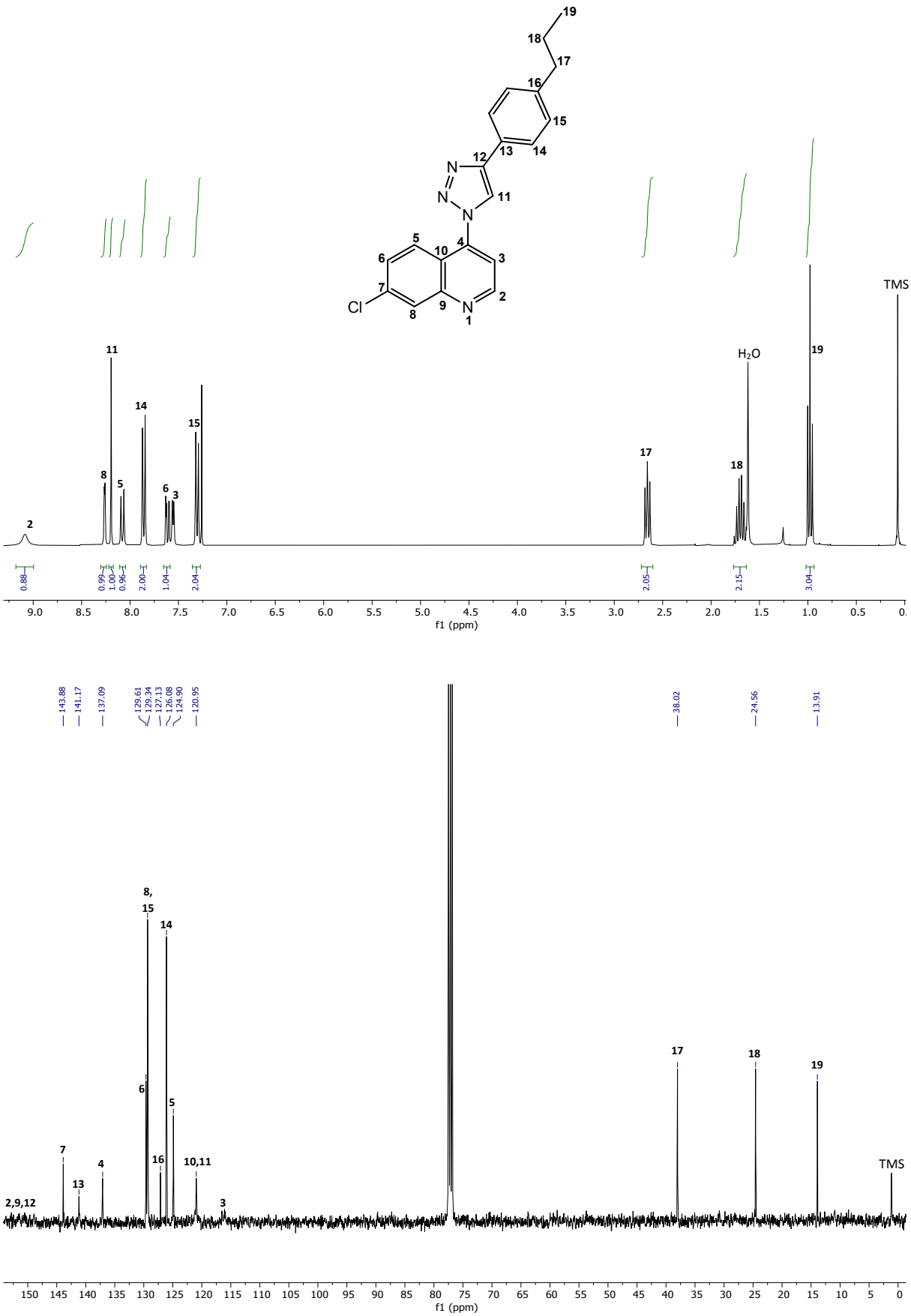

Figure S3: ^{1}H and $^{13}C\{^{1}H\}$ NMR spectra of **2c** in $CDCl_3$.

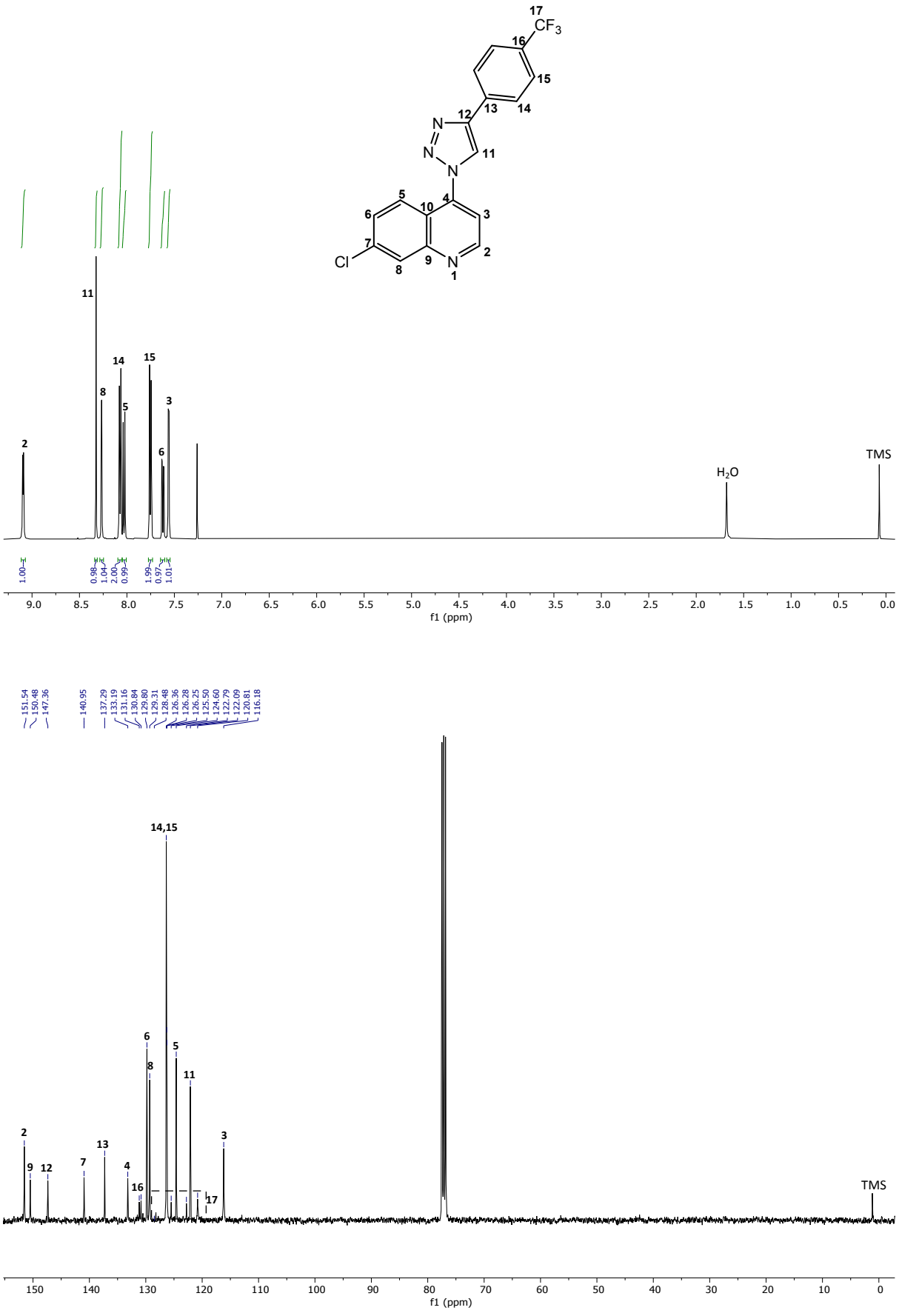

Figure S4: ^{1}H and $^{13}C\{^{1}H\}$ NMR spectra of **2d** in $CDCl_3$.

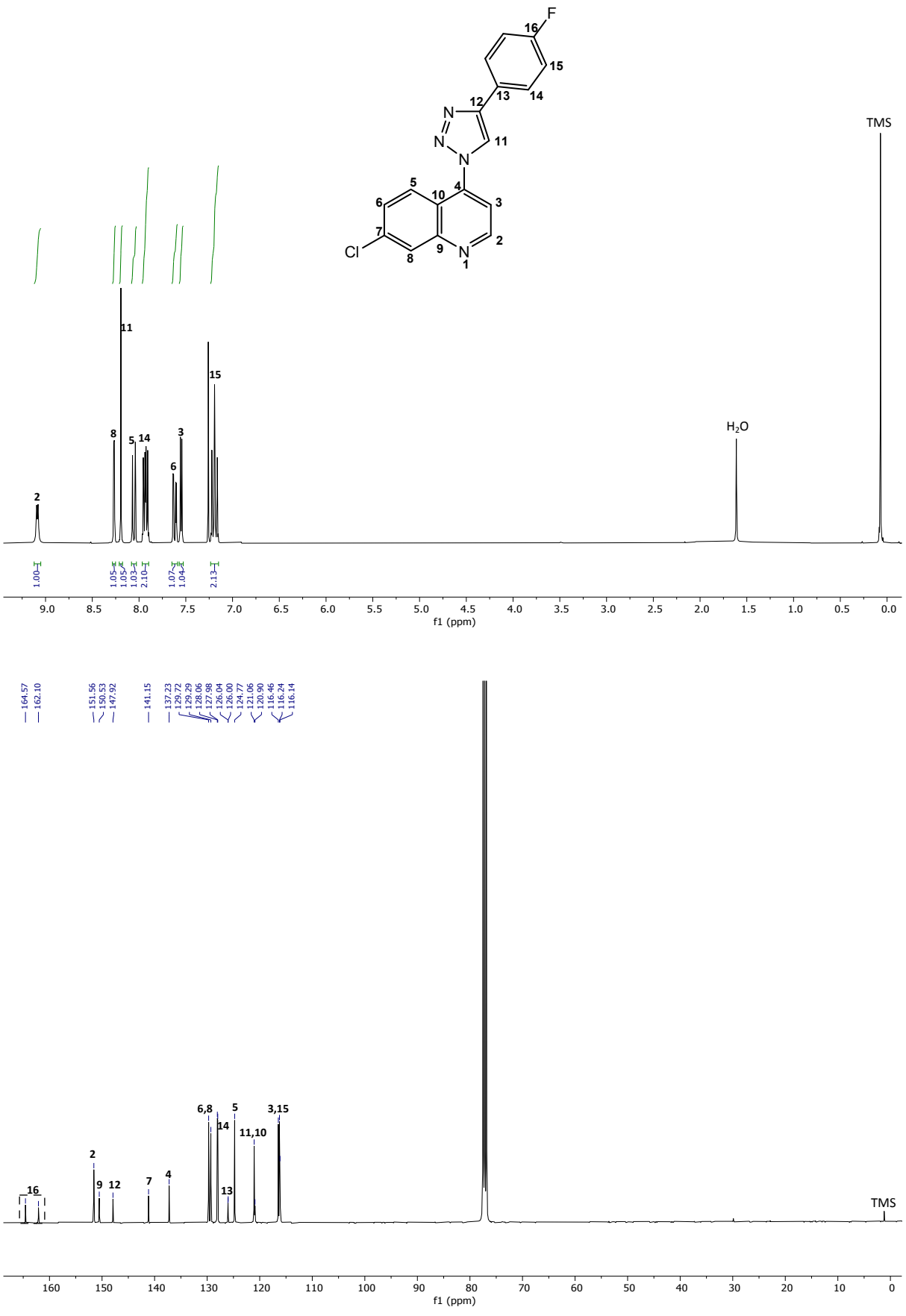

Figure S5: ^{1}H and $^{13}C\{^{1}H\}$ NMR spectra of **2e** in $CDCl_3$.

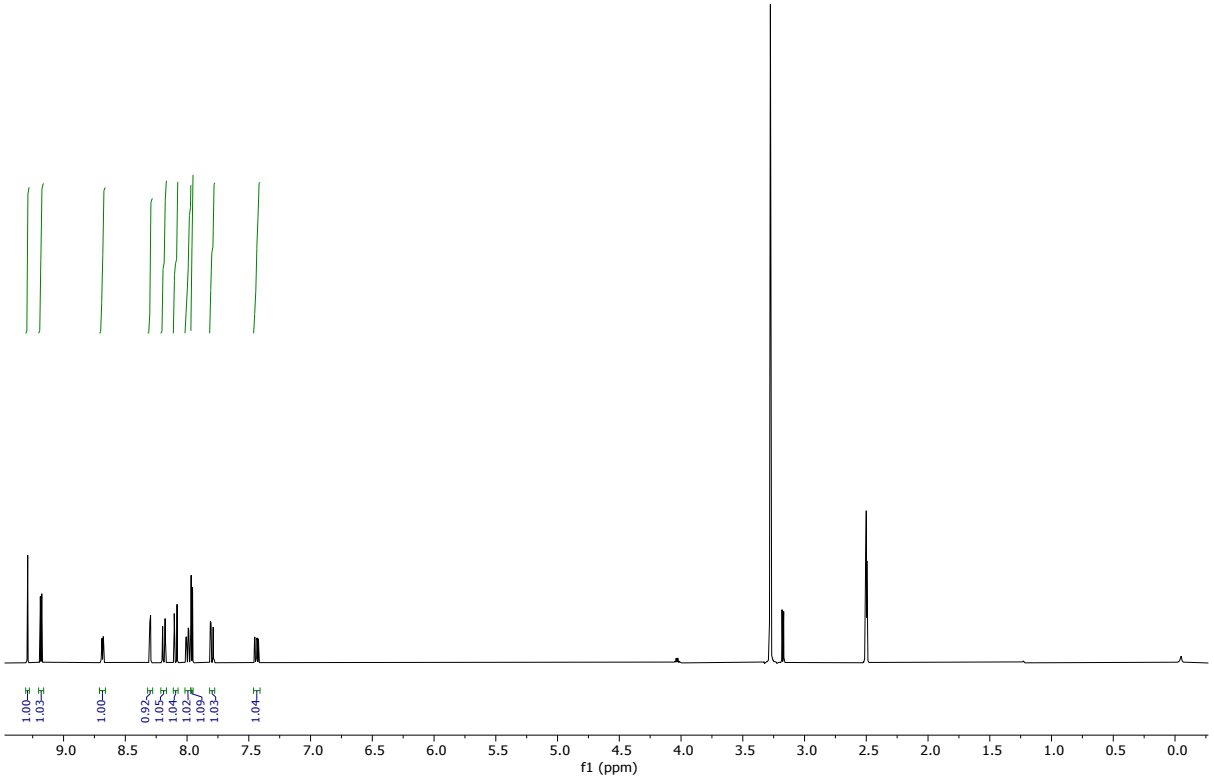
1.00
1.03
1.00
0.92
1.05
1.04
1.02
1.09
1.03
1.04
9.0
8.5
8.0
7.5
7.0
6.5
6.0
5.5
5.0
4.5
4.0
3.5
3.0
2.5
2.0
1.5
1.0
0.5
0.0
f1 (ppm)

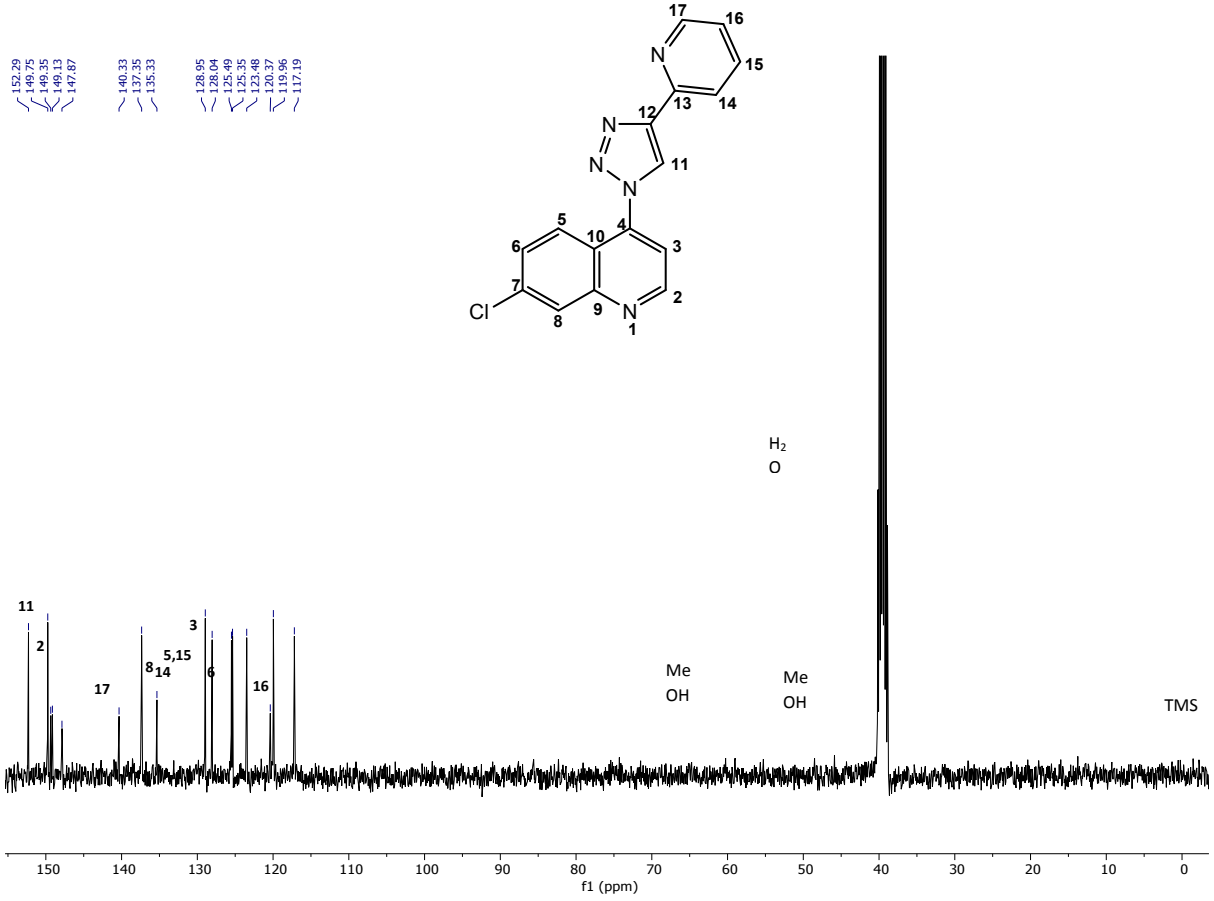
152.29
149.75
149.35
149.35
149.13
147.87
140.33
137.35
135.33
128.95
128.04
125.49
125.35
123.48
120.37
119.96
117.19
N
N
N
N
Cl
1
2
3
4
5
6
7
8
9
10
11
12
13
14
15
16
17
H2O
Me
OH
Me
OH
TMS
11
2
17
8
14
5,15
3
6
16
150
140
130
120
110
100
90
80
70
60
50
40
30
20
10
0
f1 (ppm)

Figure S6: ^{1}H and $^{13}C\{^{1}H\}$ NMR spectra of **2f** in DMSO-d_6.

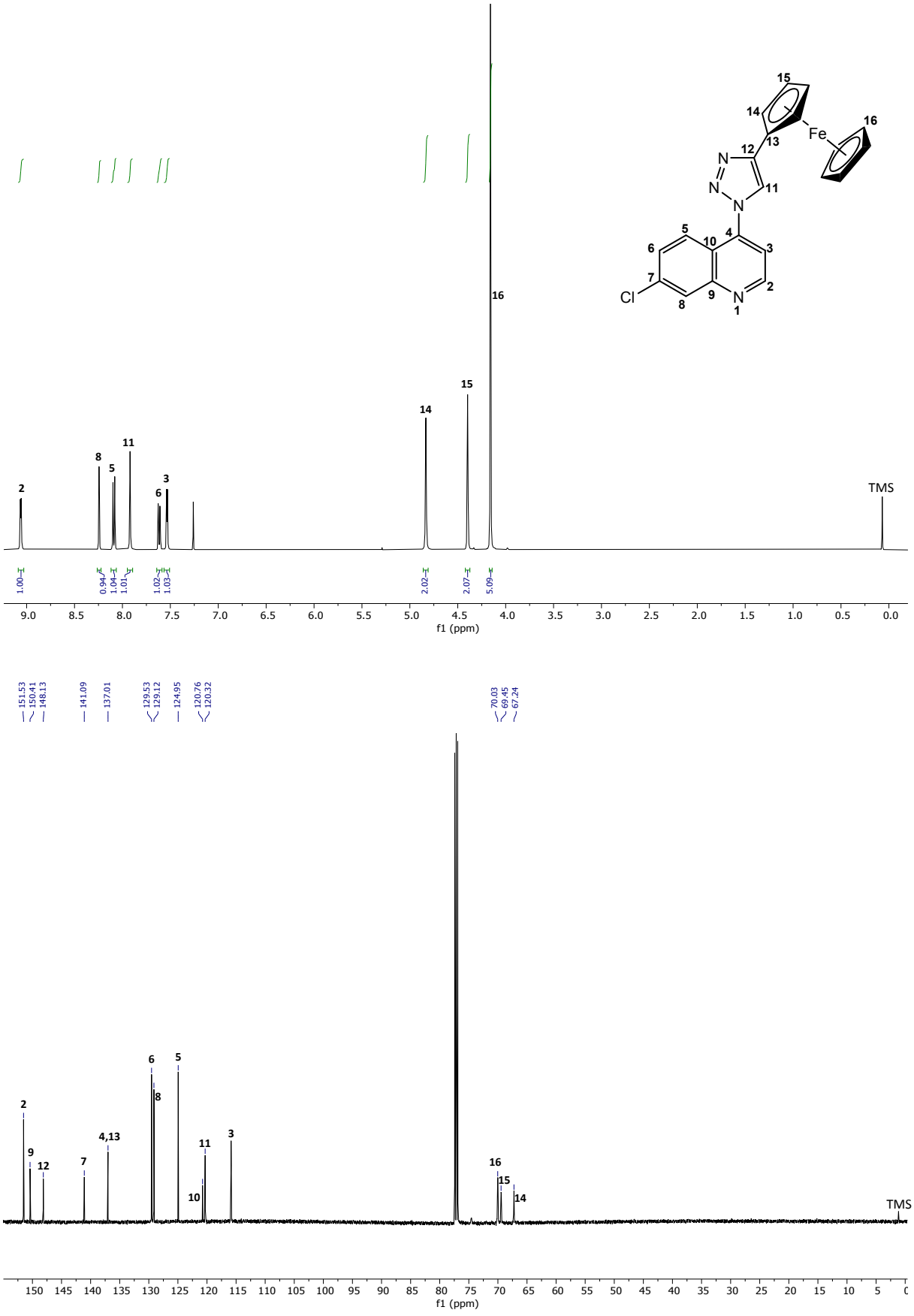

Figure S7: ^{1}H and $^{13}C\{^{1}H\}$ NMR spectra of **2g** in $CDCl_3$.

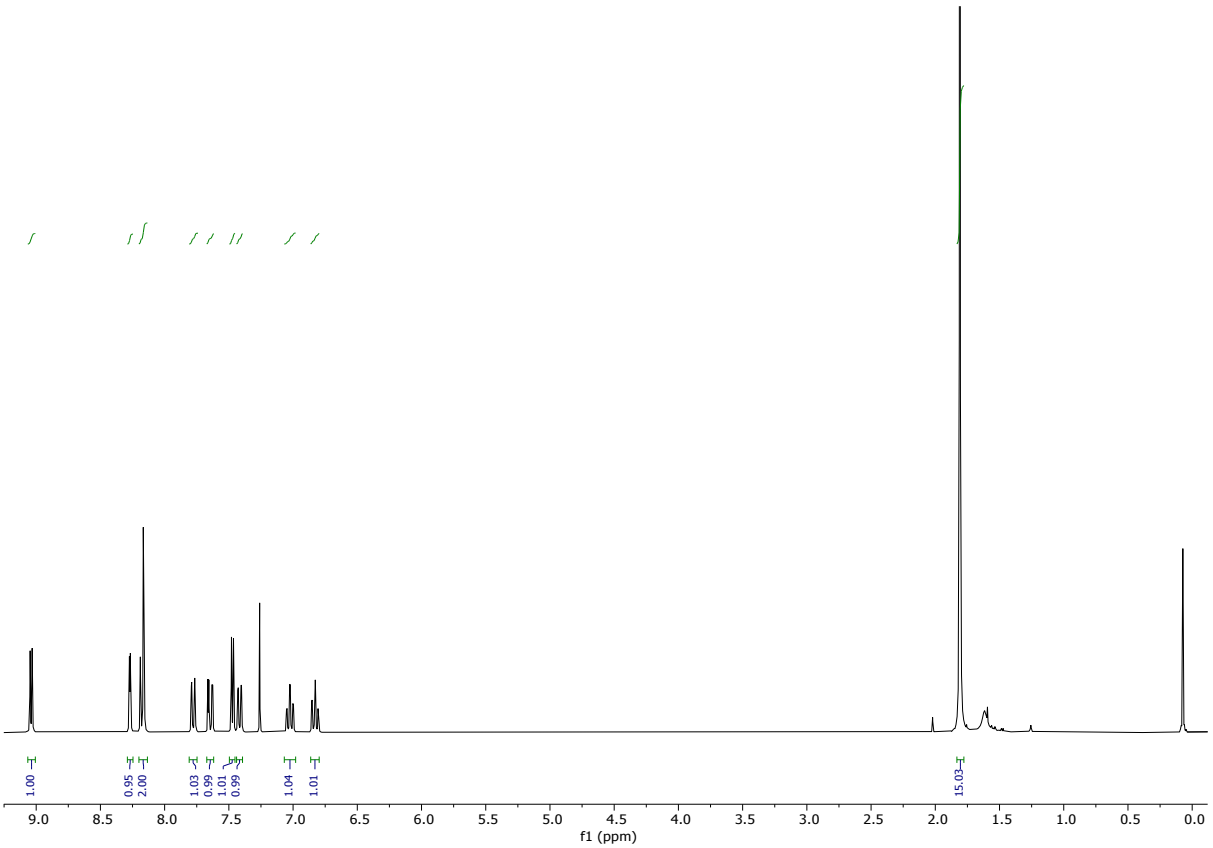
1.00
0.95
2.00
1.03
0.99
1.01
0.99
1.04
1.01
15.03
9.0 8.5 8.0 7.5 7.0 6.5 6.0 5.5 5.0 4.5 4.0 3.5 3.0 2.5 2.0 1.5 1.0 0.5 0.0
f1 (ppm)

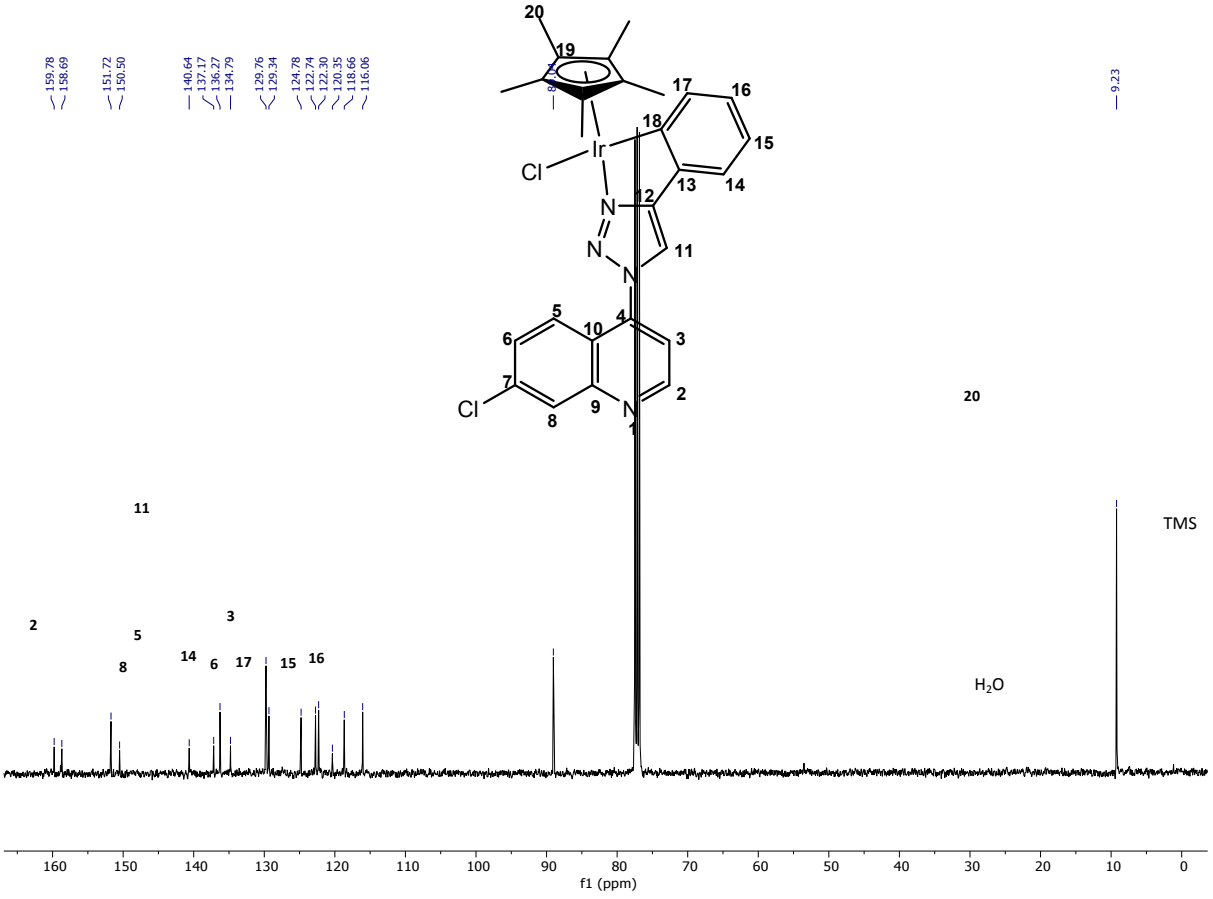
159.78
158.69
151.72
150.50
140.64
137.17
136.27
134.79
129.76
129.34
124.78
122.74
122.30
120.35
118.66
116.06
9.23
20
19
17
16
18
15
Ir
Cl
13
14
12
N
N
N
11
5
10
4
6
3
7
2
Cl
8
9
N
1
20
11
TMS
2
3
5
14
6
17
15
16
8
H2O
160 150 140 130 120 110 100 90 80 70 60 50 40 30 20 10 0
f1 (ppm)

Figure S8: ^{1}H and $^{13}C\{^{1}H\}$ NMR spectra of **3a** in $CDCl_3$.

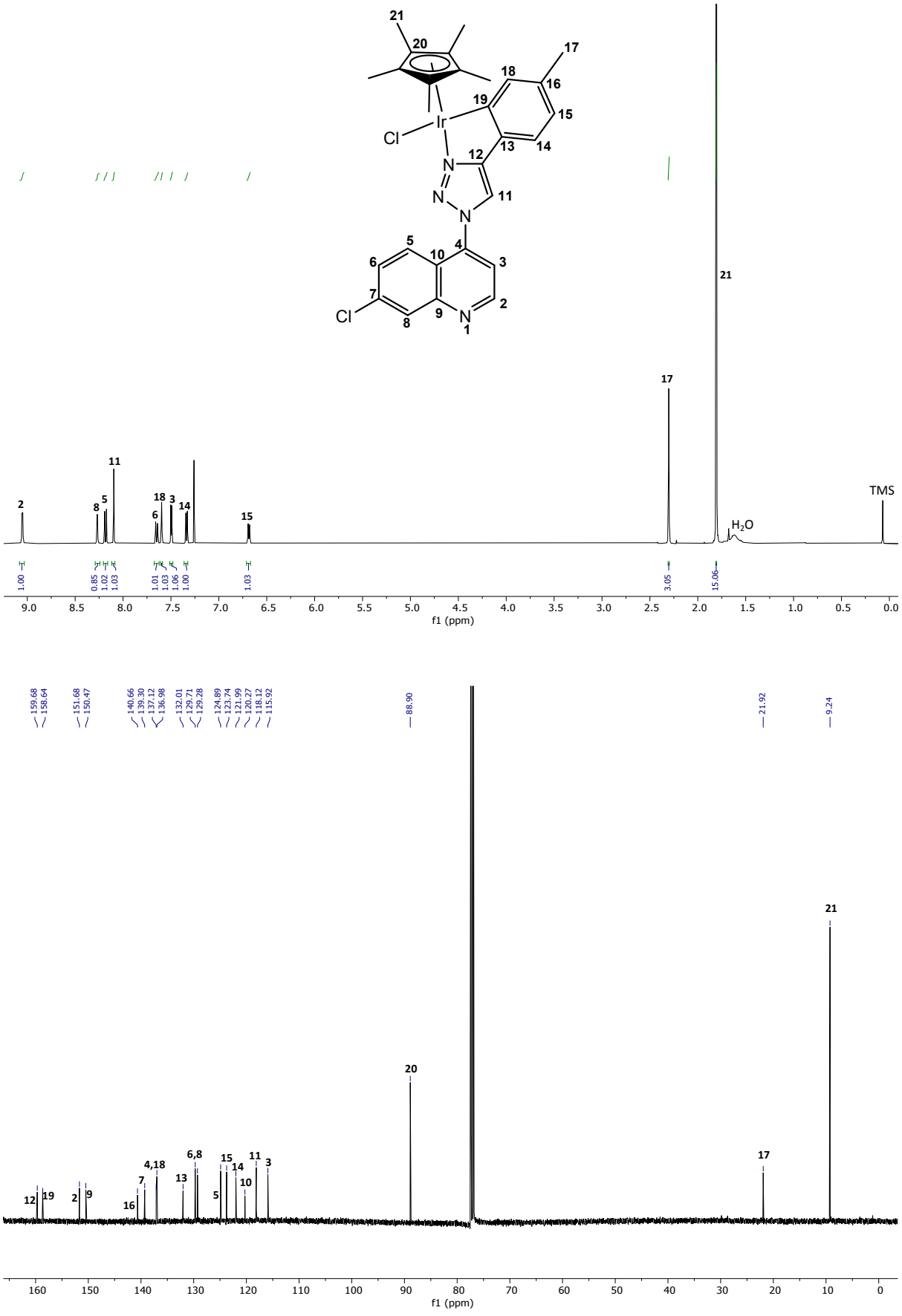

Figure S9: ^{1}H and $^{13}C\{^{1}H\}$ NMR spectra of **3b** in $CDCl_3$.

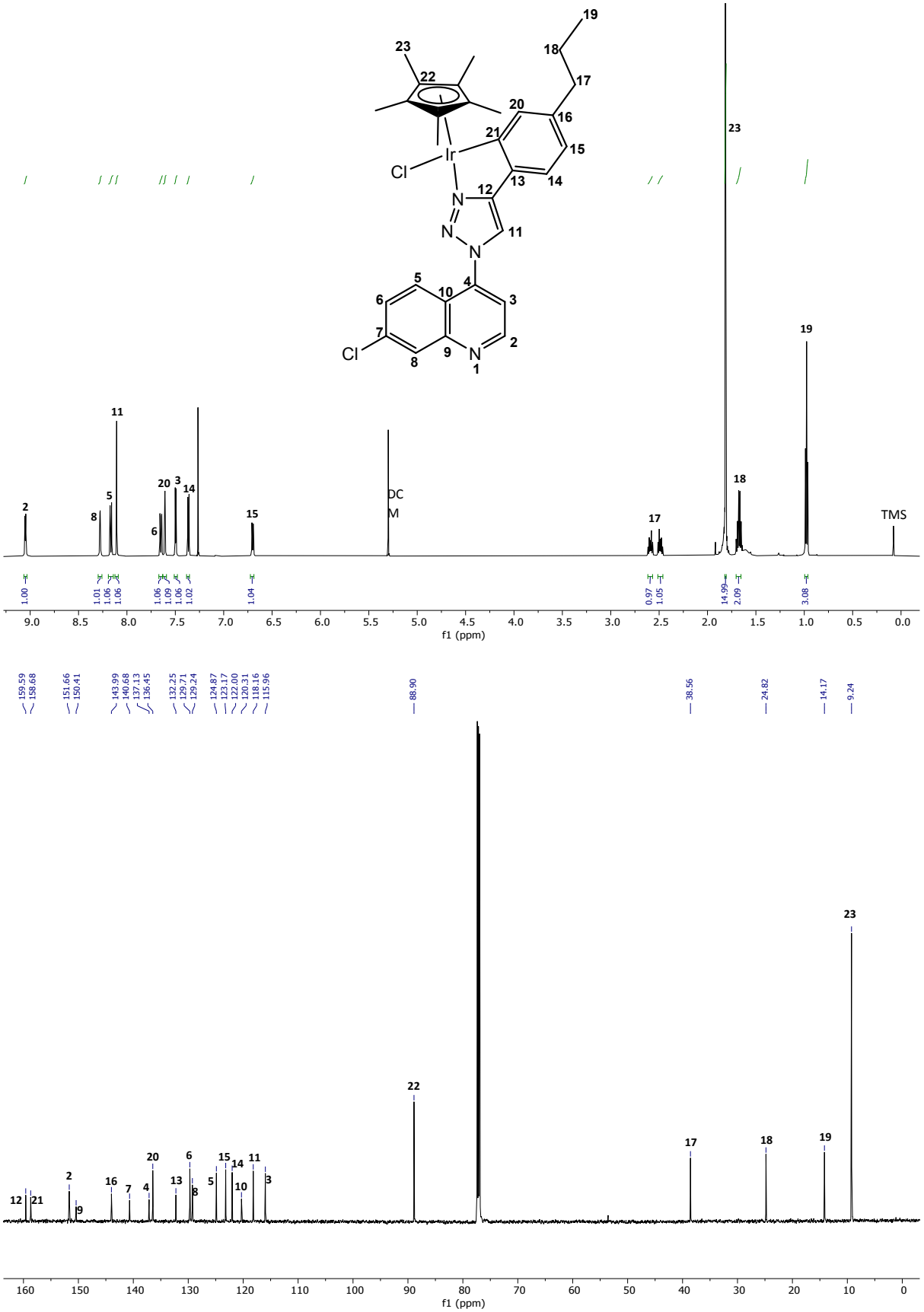

Figure S10: ^{1}H and $^{13}C\{^{1}H\}$ NMR spectra of **3c** in $CDCl_3$.

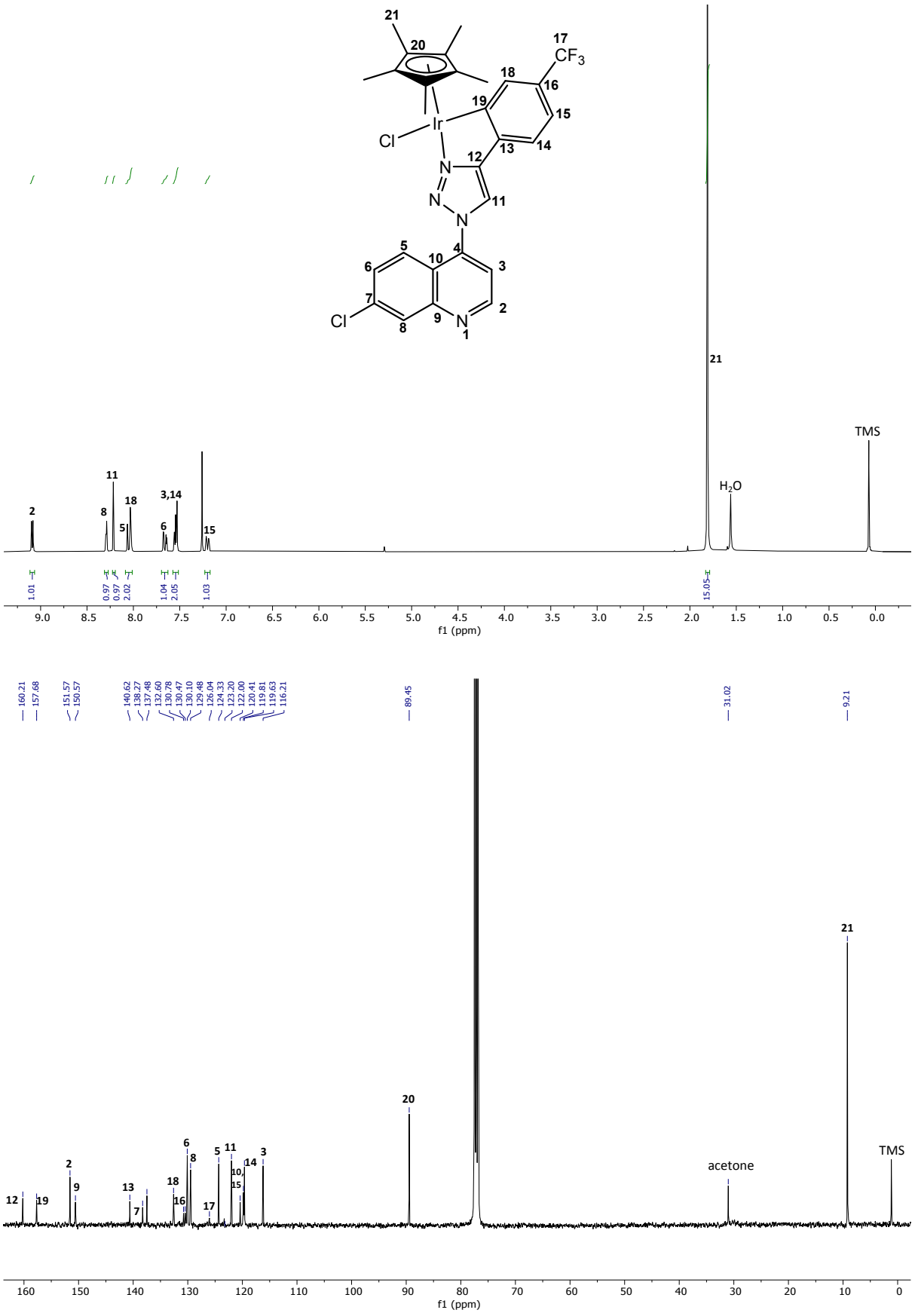

Figure S11: ^{1}H and $^{13}C\{^{1}H\}$ NMR spectra of **3d** in $CDCl_3$.

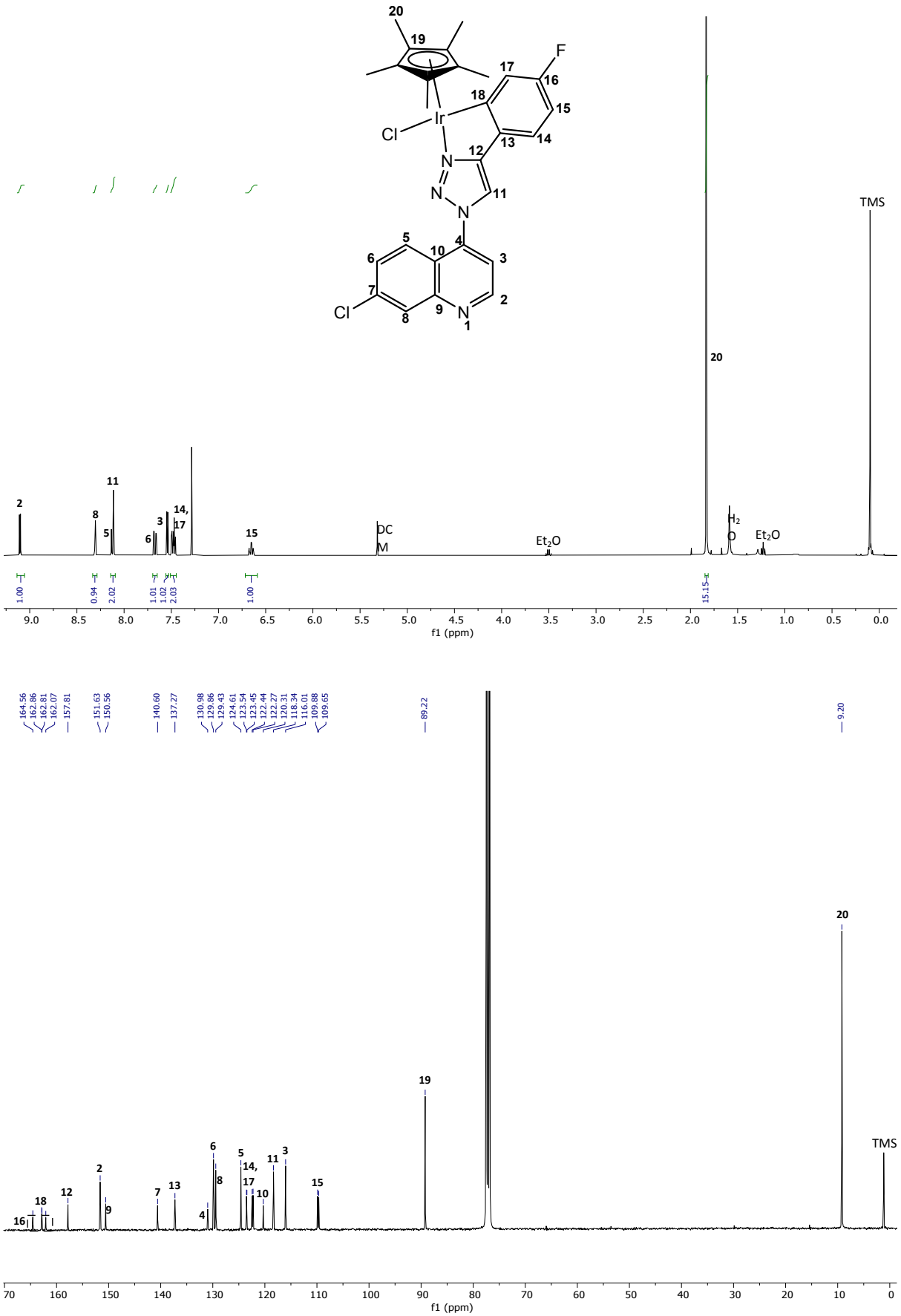

Figure S12: ^{1}H and $^{13}C\{^{1}H\}$ NMR spectra of **3e** in $CDCl_3$.

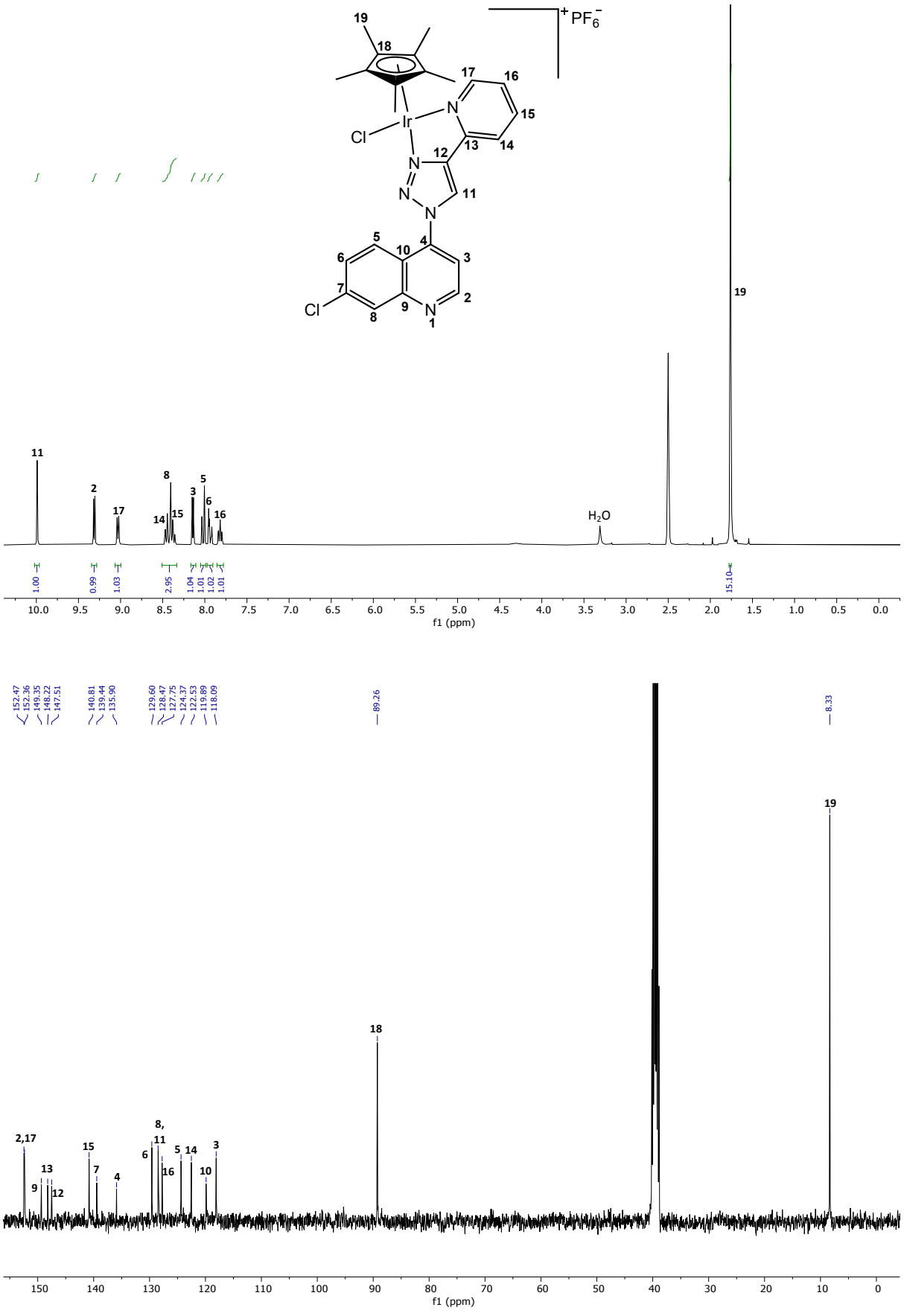

Figure S13: ^{1}H and $^{13}C\{^{1}H\}$ NMR spectra of **3f** in DMSO-d_6.

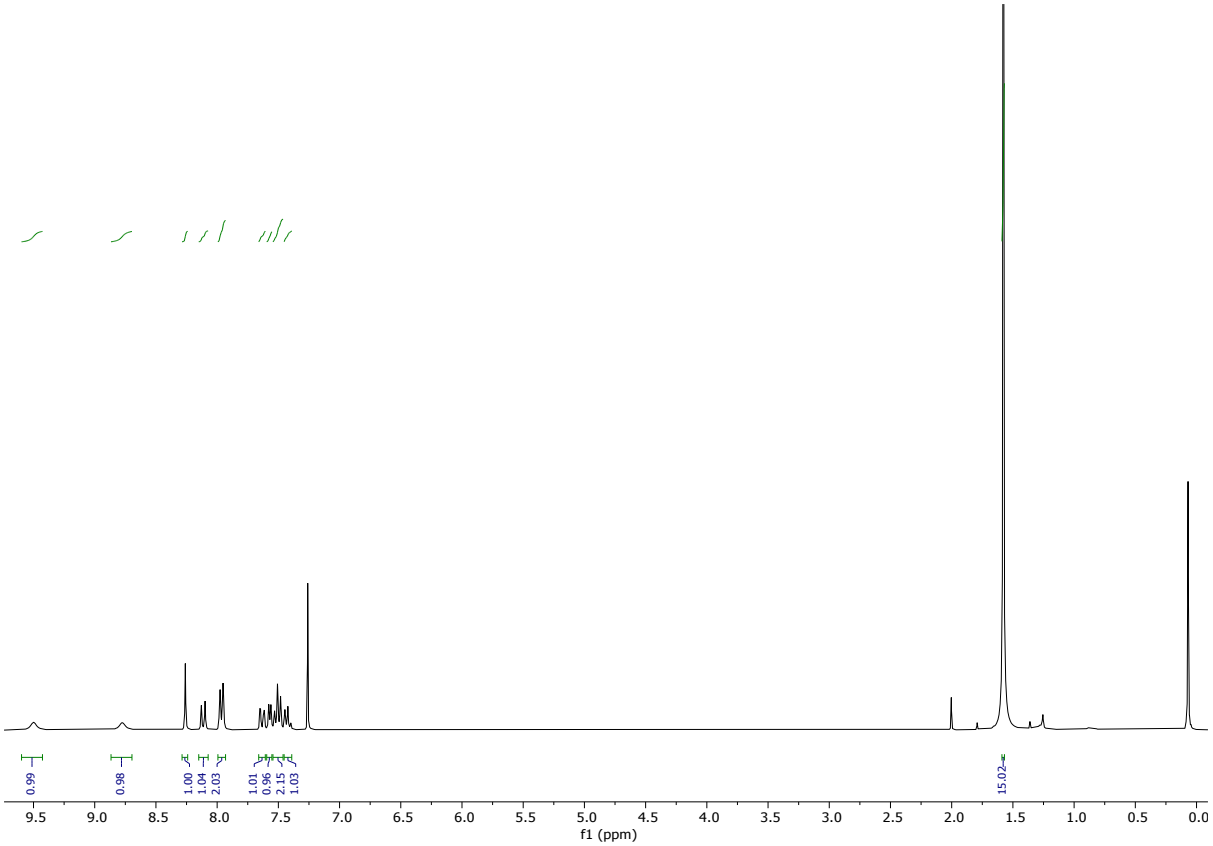
0.99
0.98
1.00
1.04
2.03
1.01
0.96
2.15
1.03
15.02
9.5 9.0 8.5 8.0 7.5 7.0 6.5 6.0 5.5 5.0 4.5 4.0 3.5 3.0 2.5 2.0 1.5 1.0 0.5 0.0
f1 (ppm)

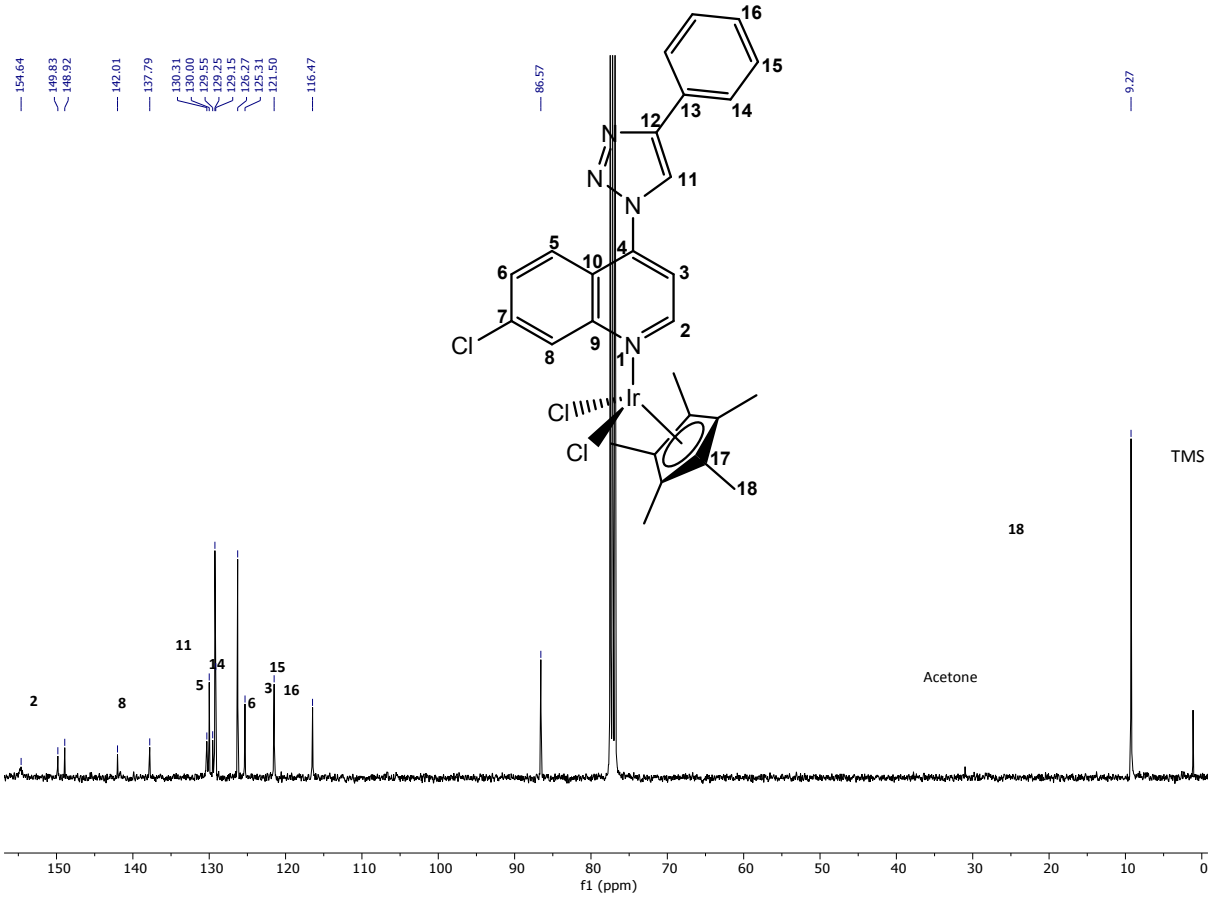
154.64
149.83
148.92
142.01
137.79
130.31
130.00
129.55
129.25
129.15
126.27
125.31
121.50
116.47
86.57
9.27
16
15
14
13
12
11
N
N
N
5
4
10
6
3
7
2
Cl
8
9
N
1
Ir
Cl
Cl
17
18
TMS
18
11
14
15
5
3
16
6
2
8
Acetone
150 140 130 120 110 100 90 80 70 60 50 40 30 20 10 0
f1 (ppm)

Figure S14: ^{1}H and $^{13}C\{^{1}H\}$ NMR spectra of **4** in $CDCl_3$.

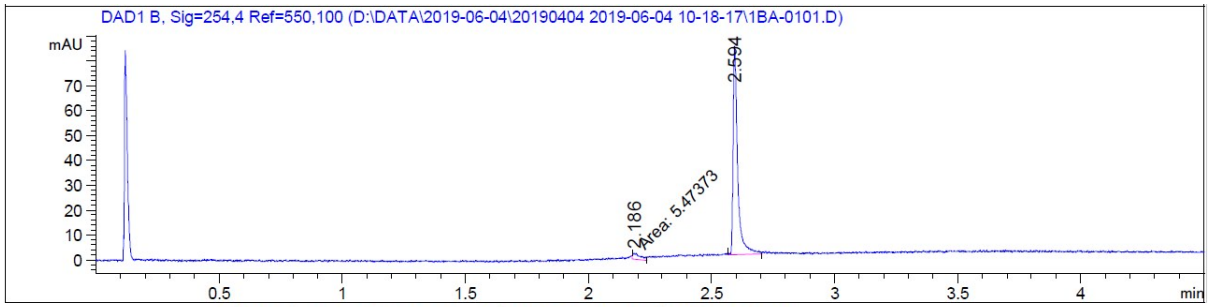

Signal 2: DAD1 B, Sig=254,4 Ref=550,100

Peak #	RetTime [min]	Type	Width [min]	Area [mAU*s]	Height [mAU]	Area %
1	2.186	MM	0.0383	5.47373	2.38028	4.7954
2	2.594	VV	0.0186	108.67117	83.75558	95.2046
Totals :				114.14490	86.13586	

Figure S15: Purity by LCMS of **2a**.

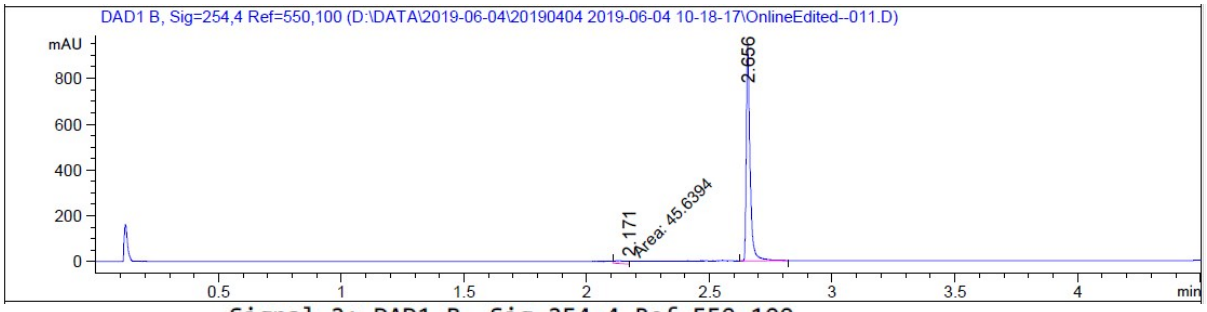

Signal 2: DAD1 B, Sig=254,4 Ref=550,100

Peak #	RetTime [min]	Type	Width [min]	Area [mAU*s]	Height [mAU]	Area %
1	2.171	MM	0.0594	45.63942	12.80264	4.2766
2	2.656	BV	0.0162	1021.55823	935.88043	95.7234
Totals :				1067.19765	948.68307	

Figure S16: Purity by LCMS of **2b**.

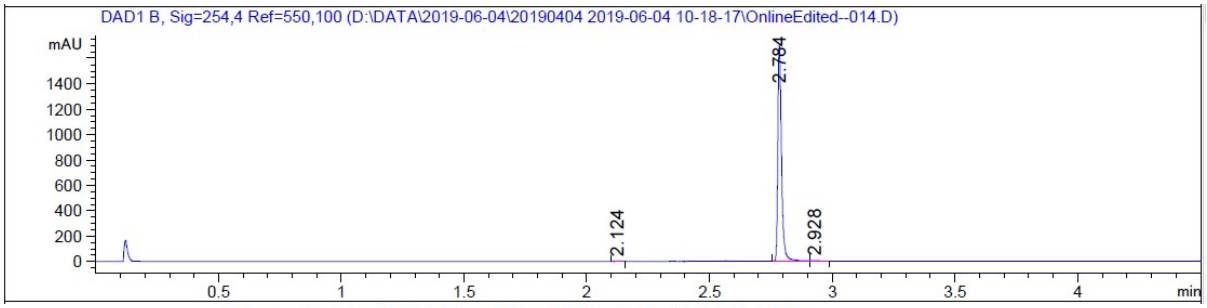

Signal 2: DAD1 B, Sig=254,4 Ref=550,100

Peak #	RetTime [min]	Type	Width [min]	Area [mAU*s]	Height [mAU]	Area %
1	2.124	VV	0.0275	5.83512	2.66571	0.3250
2	2.784	BV	0.0158	1782.15259	1691.24084	99.2549
3	2.928	VB	0.0313	7.54264	3.10419	0.4201
Totals :				1795.53035	1697.01075	

Figure S17: Purity by LCMS of **2c**.

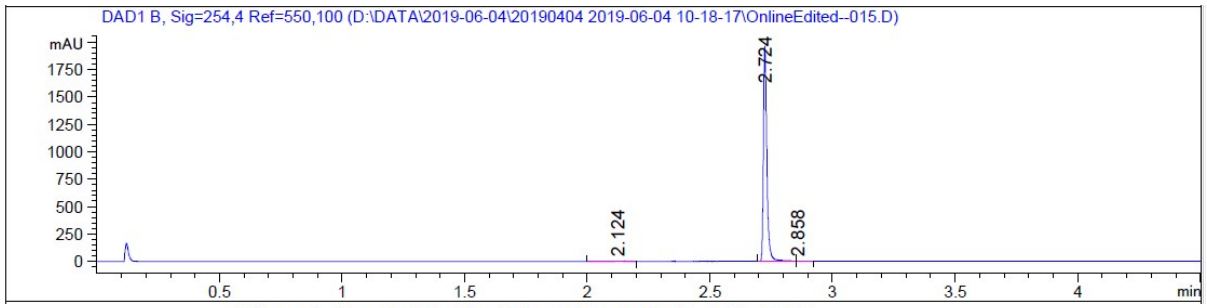

Signal 2: DAD1 B, Sig=254,4 Ref=550,100

Peak #	RetTime [min]	Type	Width [min]	Area [mAU*s]	Height [mAU]	Area %
1	2.124	VV	0.0442	10.03746	2.74075	0.5174
2	2.724	BV	0.0150	1923.61304	1947.41528	99.1506
3	2.858	VV	0.0306	6.44185	2.58458	0.3320
Totals :				1940.09235	1952.74062	

Figure S18: Purity by LCMS of **2d**.

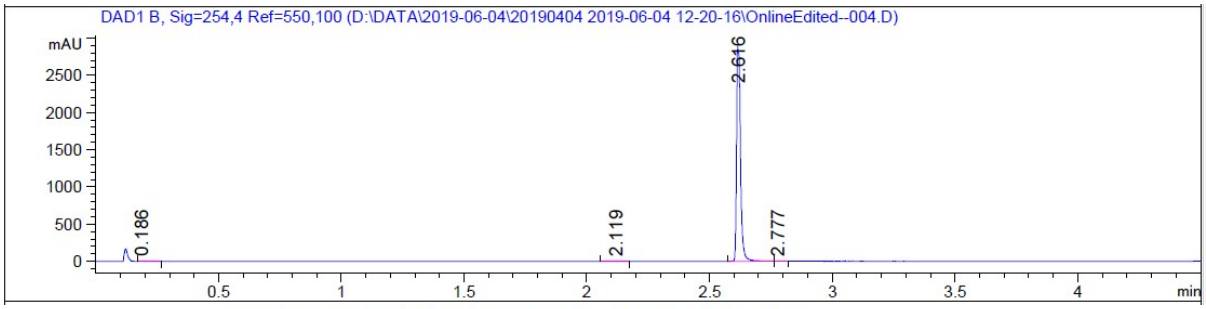

Signal 2: DAD1 B, Sig=254,4 Ref=550,100

Peak #	RetTime [min]	Type	Width [min]	Area [mAU*s]	Height [mAU]	Area %
1	0.186	VB	0.0327	11.44019	4.42404	0.3537
2	2.119	VV	0.0383	7.44550	2.42715	0.2302
3	2.616	BV	0.0171	3208.91064	2856.87354	99.1979
4	2.777	VV	0.0294	7.06062	3.18246	0.2183
Totals :				3234.85695	2866.90719	

Figure S19: Purity by LCMS of **2e**.

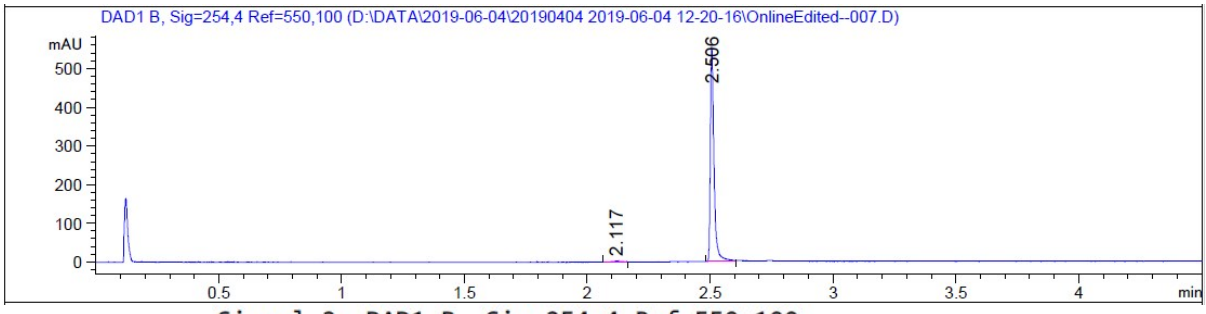

Signal 2: DAD1 B, Sig=254,4 Ref=550,100

Peak #	RetTime [min]	Type	Width [min]	Area [mAU*s]	Height [mAU]	Area %
1	2.117	VV	0.0356	7.76866	2.66153	1.3405
2	2.506	BV	0.0155	571.75751	555.30829	98.6595
Totals :				579.52617	557.96982	

Figure S20: Purity by LCMS of **2f**.

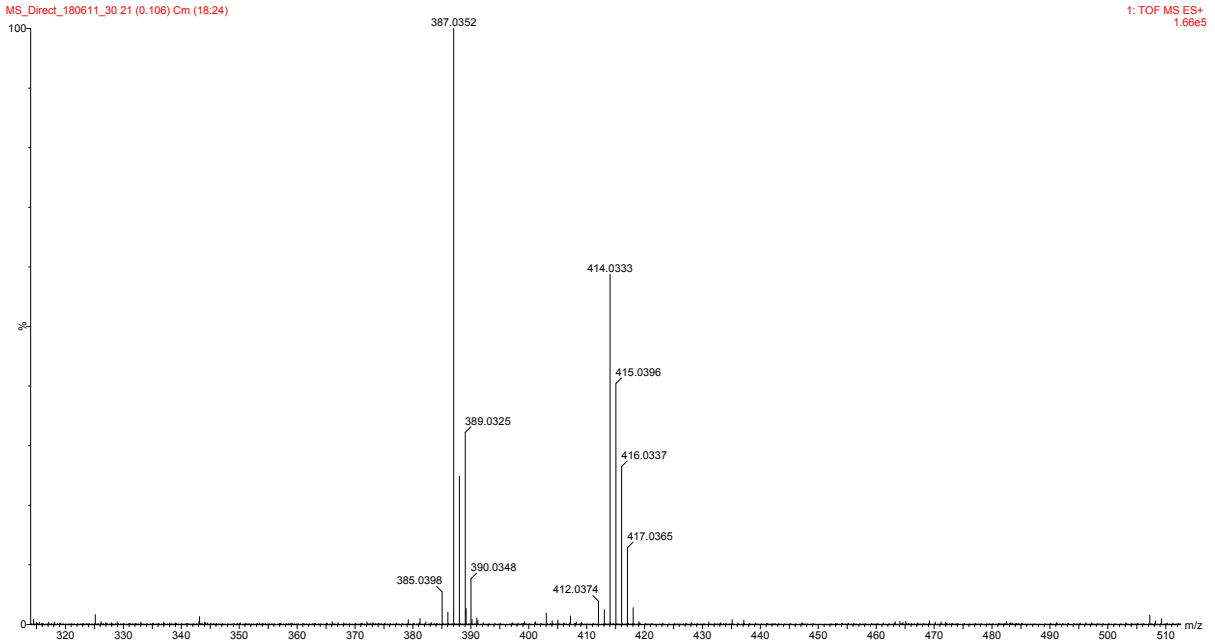

Figure S21: ESI-Mass Spectrum of **2g**.

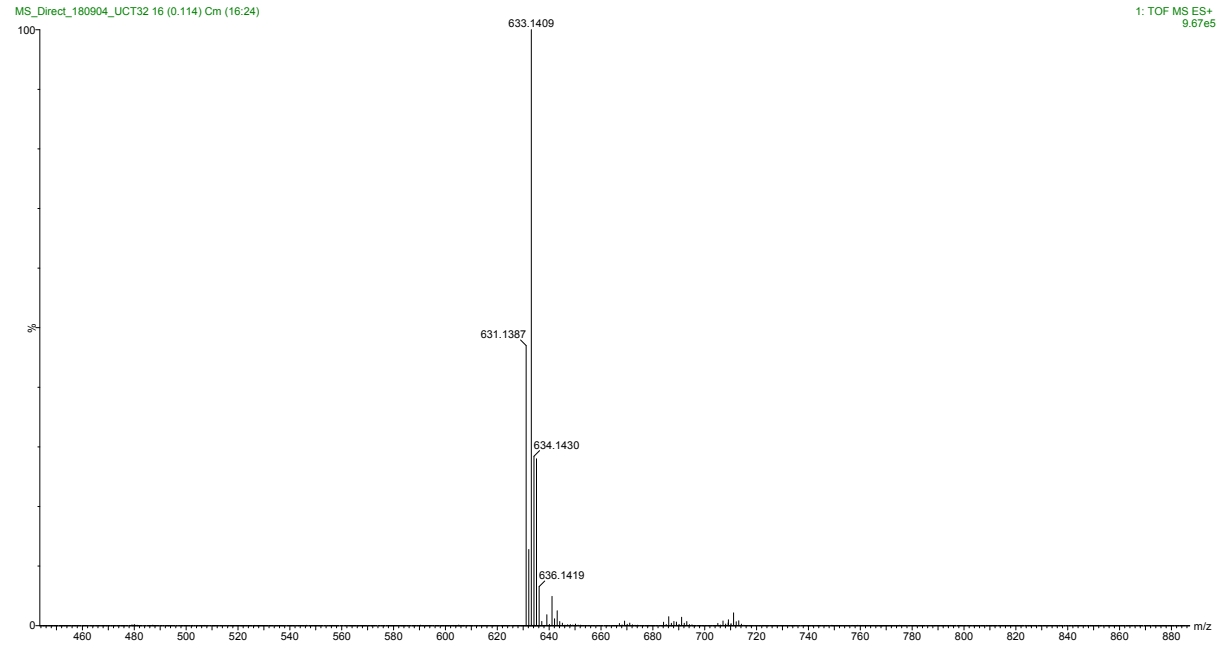

Figure S22: ESI-Mass Spectrum of **3a**.

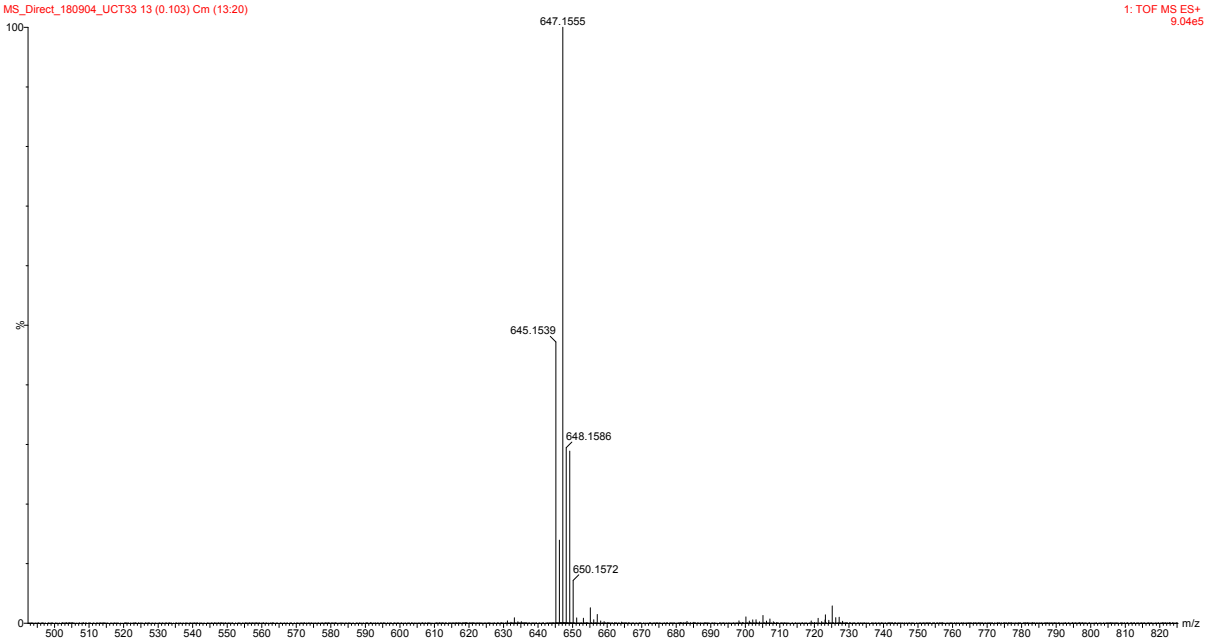

Figure S23: ESI-Mass Spectrum of **3b**.

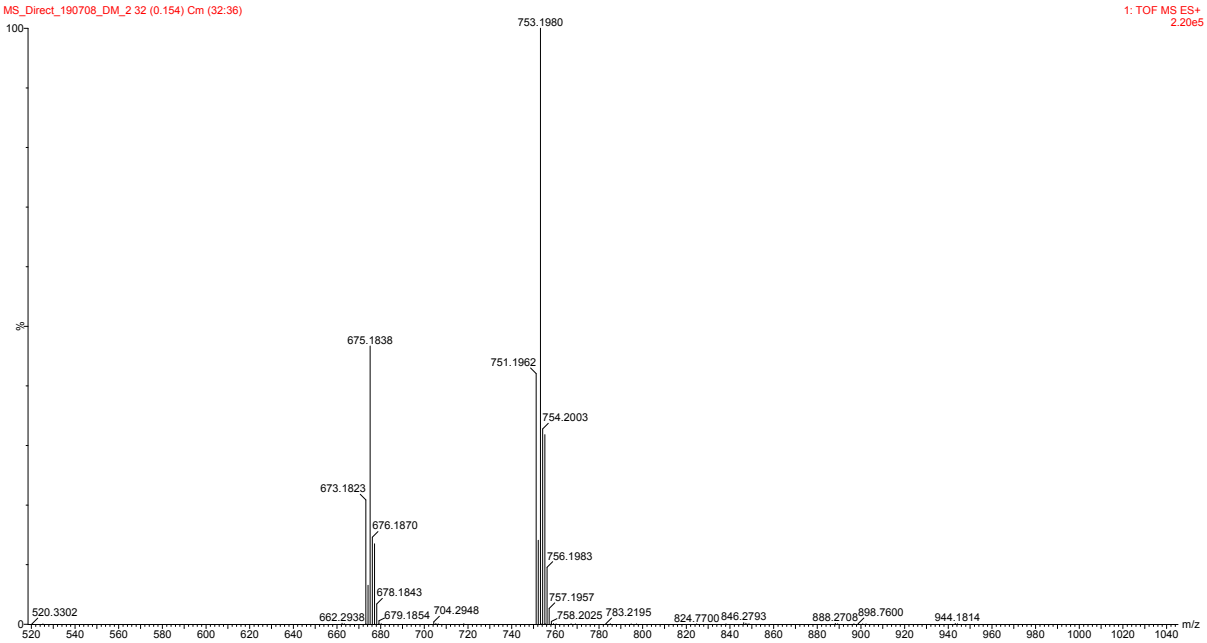

Figure S24: ESI-Mass Spectrum of **3c**.

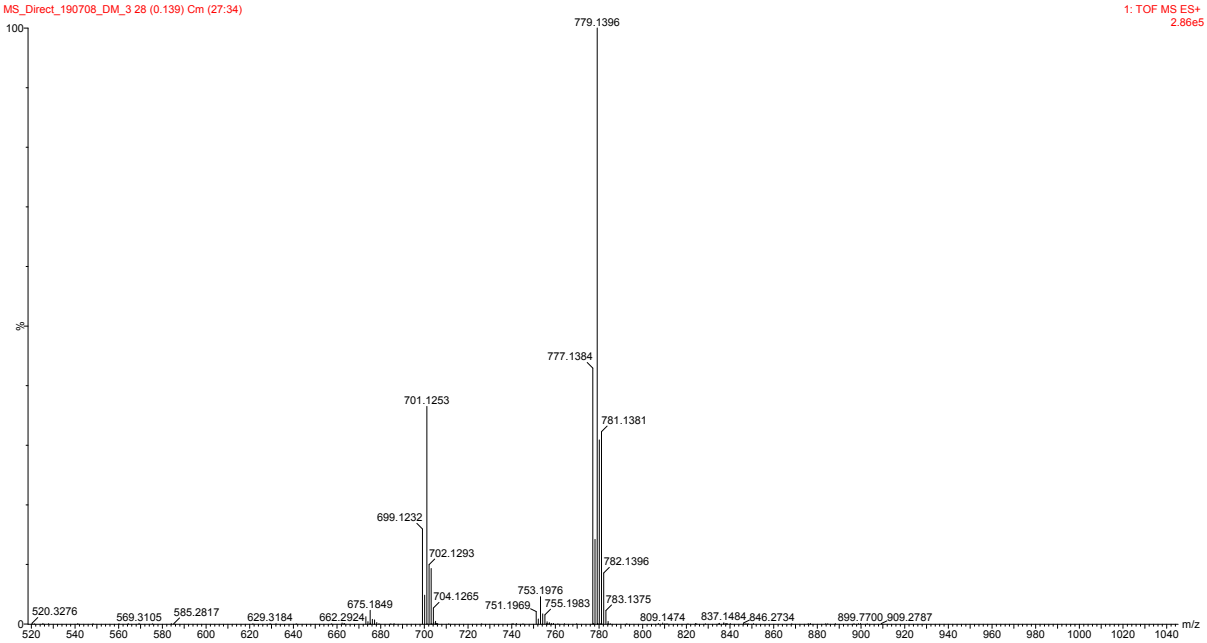

Figure S25: ESI-Mass Spectrum of **3d**.

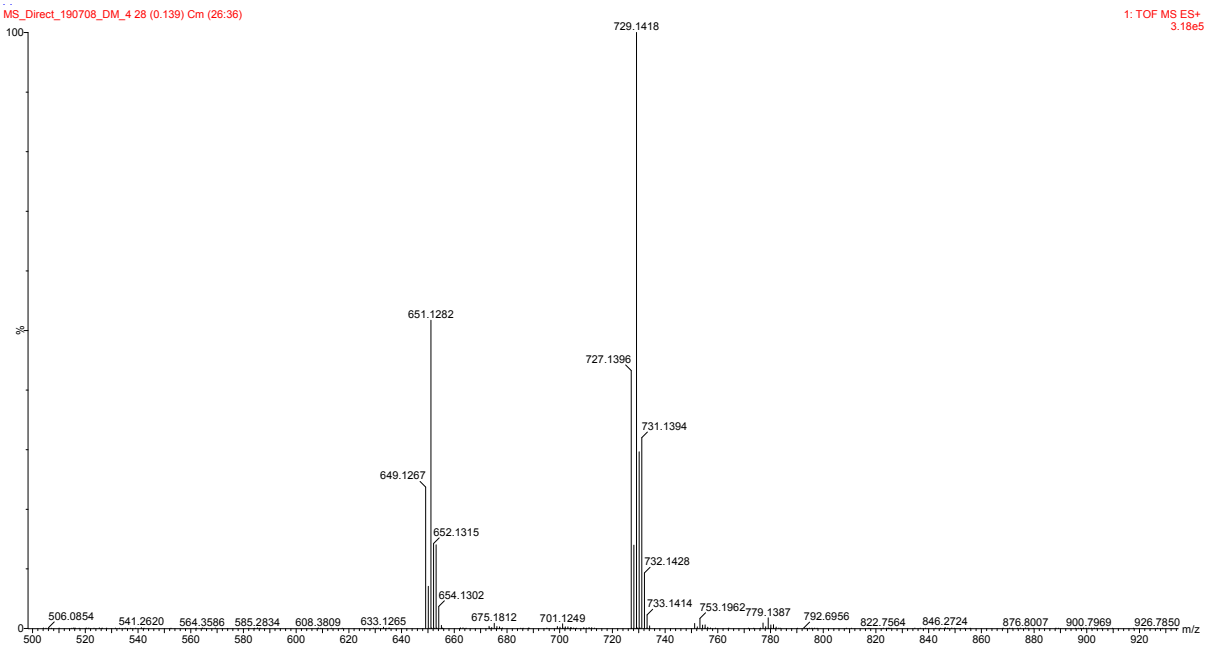

Figure S26: ESI-Mass Spectrum of **3e**.

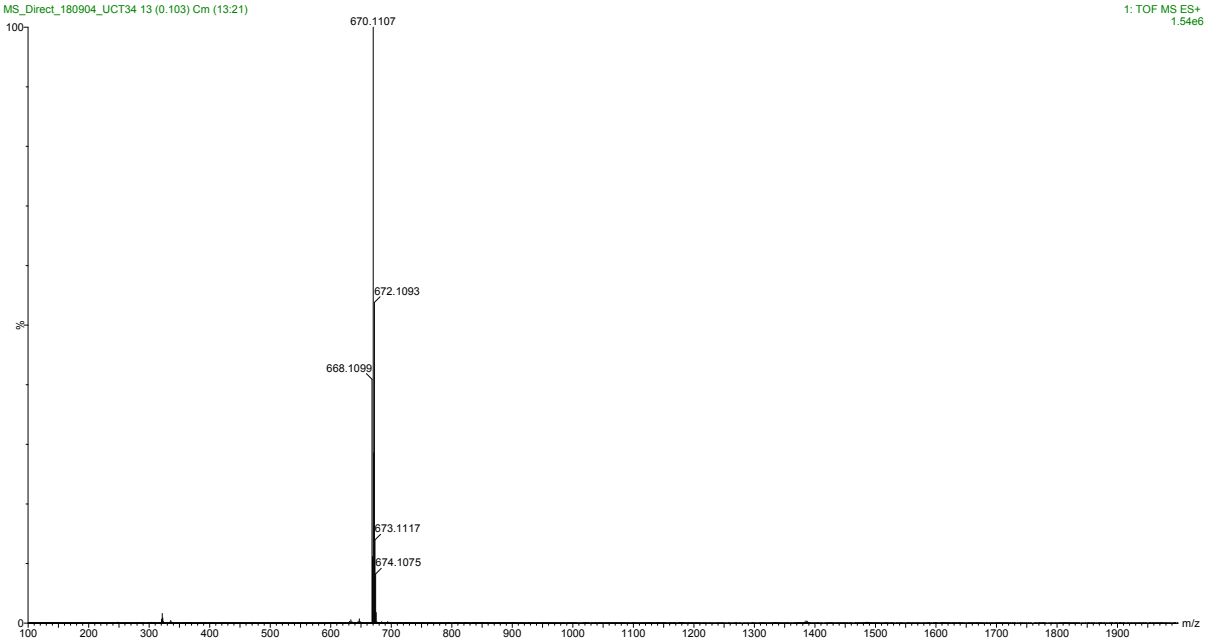

Figure S27: ESI-Mass Spectrum of **3f**.

Table S1 Crystallographic data and refinement parameters for complexes **3a** and **4**.

	Complex 3a	**Complex 4**
Chemical formula	$C_{27}H_{25}Cl_2IrN_4$	$C_{27}H_{26}Cl_3IrN_4$
Formula weight	668.63	705.09
Crystal system	monoclinic	orthorhombic
Space group	$P2_1/c$ (No. 14)	Pbca (No. 61)
a, b, c (Å)	12.6578(13), 7.9469(9), 24.600(3)	7.9369(5), 22.7369(14), 28.4099(16)
α, β, γ (°)	90, 97.192(3), 90	-
V (Å^3)	2455.1(5)	5126.9(5)
Z	4	8
D (g.cm^{-3})	1.809	1.827
μ (mm^{-1})	5.680	5.546
F (000)	1304	2752
Crystal size (mm)	0.03 x 0.07 x 0.09	0.07 x 0.08 x 0.09
T (K)	173	173
Scan range (°)	1.7 < θ < 28.4	1.4 < θ < 28.4
Unique reflections	6162	6441
R_{int}	0.110	0.121
Reflections used [I>2σ(I)]	4783	4775
R indices (all data)	R 0.0314, wR2 0.0682, S 1.01	R 0.0266, wR2 0.0546, S 1.01
Goodness-of-fit	1.01	1.01
Max, Min Δρ (e Å^{-3})	-1.14, 0.70	-0.63, 0.51

Table S2 Selected bond lengths and angles for iridium(III) complexes **3a** and **4**.

Complex 3a		**Complex 4**	
	Bond lengths (Å)		
Ir_1-N_1	2.071(3)	**Ir_1-N_1**	2.159(3)
Ir_1-Cl_1	2.3986(12)	**Ir_1-Cl_1**	2.4167(12)
Ir_1-C_1	2.062(4)	**Ir_1-Cl_2**	2.3952(9)
	Bond angles (°)		
Cl_1-Ir_1-N_1	88.39(9)	**Cl_1-Ir_1-N_1**	87.76(8)
N_1-Ir_1-C_1	77.58(14)	**Cl_2-Ir_1-N_1**	87.29(9)
Cl_1-Ir_1-C_1	85.84(11)	**Cl_1-Ir_1-Cl_2**	85.34(3)
	Torsion angles (°)		
N_1-C_7-C_6-C_1	4.6(5)	**N_4-C_{11}-C_{12}-C_{13}**	47.8(5)
C_{17}-C_9-N_3-N_2	-32.2(5)	**N_4-N_2-C_5-C_9**	22.8(6)

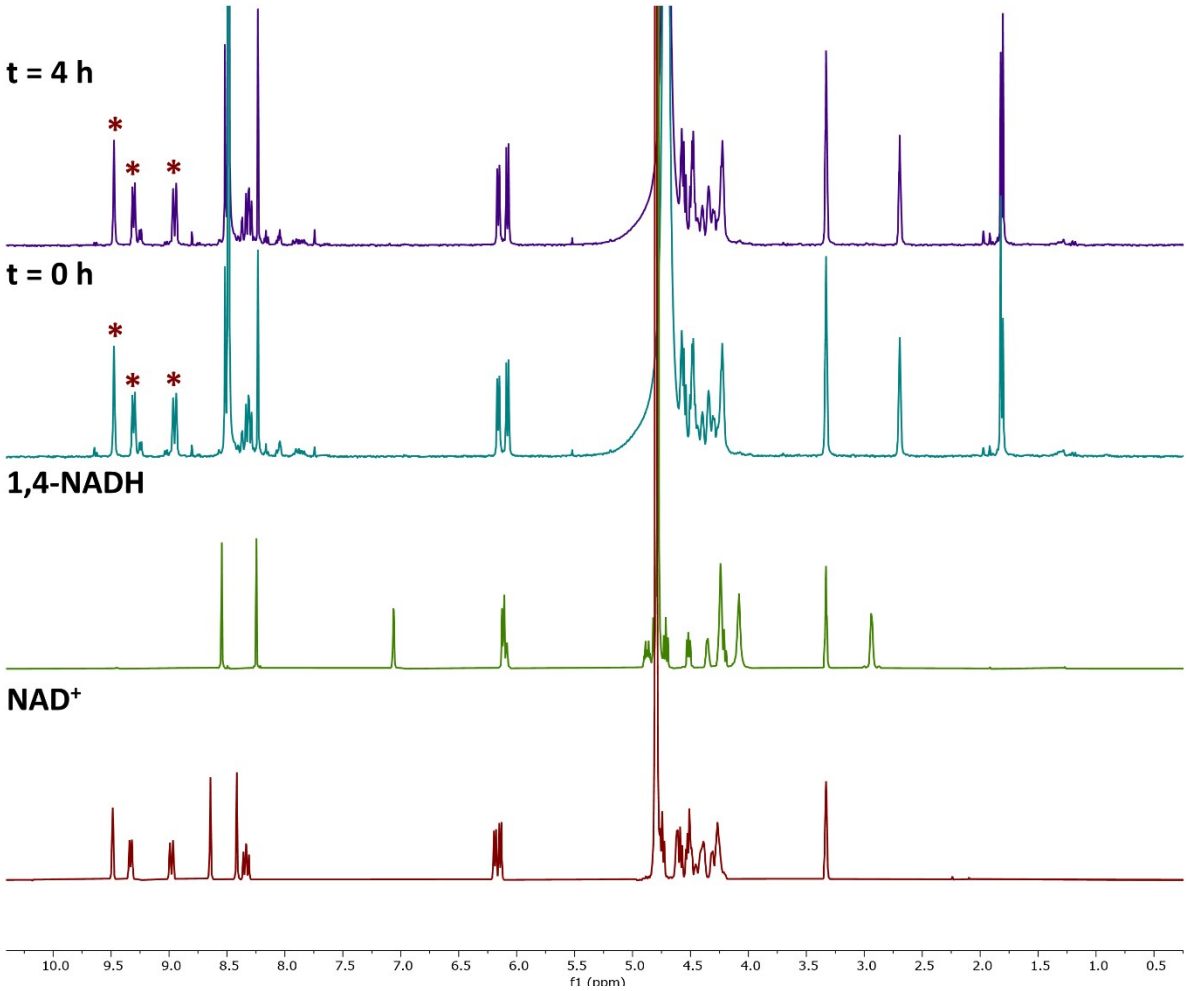

Fig. S28: ^{1}H NMR spectra of a mixture of cationic Ir(III) complex **3f**, NAD^+ and sodium formate in MeOD/D_2O at 37 °C, showing no reduction to 1,4-NADH after 4 hours. Signals marked by (*) represent NAD^+.

Computational analysis

We hypothesized that the formation of the cyclometallated complexes **3a-e** proceeds via initial coordination of a triazole nitrogen to the iridium ion, followed by oxidative addition of a C-H bond and reductive elimination of HCl (or HOAc, as sodium acetate was used in the reaction). We decided to probe this hypothesis via computational simulations and to probe kinetic (monodentate quinoline coordination) versus thermodynamic (cyclometallated) control taking place during the synthesis of iridium(III) complexes **3a-e**. Two computational methods were used, namely, optimisation to find a stationary point and a relaxed geometry scan to scan the Ir-N bond length. The ORCA software (v 4.1.1)[41] was used and dispersion-corrected DFT was chosen as the level of theory,[42] specifically the BLYP-D3 method with def2-SVP as a basis and def2-ECP as an effective core potential. Optimisations were carried out; frequencies and molecular orbitals were calculated, and scans were carried out with the same level of theory. The labelled pathway for these studies is shown in Figure 2, detailing the reaction process from the iridium metal dimer, **I**, through plausible intermediates and ending with the characterised compounds, **IV** and **V**. Firstly, an optimisation of the cations of **IIIa** and **IIIb**, the plausible intermediates on the way to the final compounds, was carried out. The results of this study found that intermediate **IIIb**, with the iridium coordinated to the triazole nitrogen, is lower in energy than the quinoline-coordinated-Ir intermediate **IIIa** by 2 kcal/mol. While a small change, this shows that intermediate **IIIb** is already more stable than intermediate **IIIa**.

The reaction to form product **IV** or **V** from intermediate **II** and the ligand, **L**, was then investigated. The energy barrier between the reactants and the products is estimated by creating a cationic complex of **II** with the ligand, as shown in Fig. 2. A scan is carried out where the Ir-N bond is then pulled from a short bond length to several Ångströms away. This process, although modelled as the inverse of the ligand binding, represents how the ligand binds to **II**, by the principle of microscopic reversibility. A small energy barrier would be considered to lead to a kinetic product, while a larger energy barrier which leads to a lower energy product would be considered the thermodynamic route. Fig. 3 shows the outcome of the two simulations performed, one with the ligand bound to the metal at the quinoline nitrogen and one with the ligand binding at the triazole nitrogen. Fig. 3a shows the energy diagram for the former, illustrating that the outcome for the coordination of the metal to the quinoline nitrogen is a small energy barrier. When the distance between the Ir and quinoline nitrogen is 6.0 Å, the resulting complex structure is relatively low in energy. As the distance thereafter decreases, the energy increases until it eventually reaches an energy barrier of approximately 5 kcal/mol. At this energy, the bond forms, resulting in a higher energy complex. This energy barrier can be overcome at standard state temperature in both the forward and reverse reaction, which explains why the monodentate complex **4** is formed relatively rapidly at room temperature and suggests a kinetic product. The outcome for the latter, the coordination of the metal to the triazole nitrogen, is shown in the energy diagram in Fig. 3b. In this case, the energy barrier for the formation of the Ir-N bond is very high, with no minimum observed thus far. When the distance between the Ir and triazole nitrogen is 5.2 Å, the resulting complex structure is low in energy, however, as the distance decreases, the energy increases until it eventually reaches an energy barrier of nearly 12 kcal/mol. The higher predicted energy required to form the cyclometallated complex **3a** explains the need for the high temperature required to synthesise this product. These calculations support the hypothesis that the complex **3a** is a thermodynamic product while complex **4** is a kinetic product.

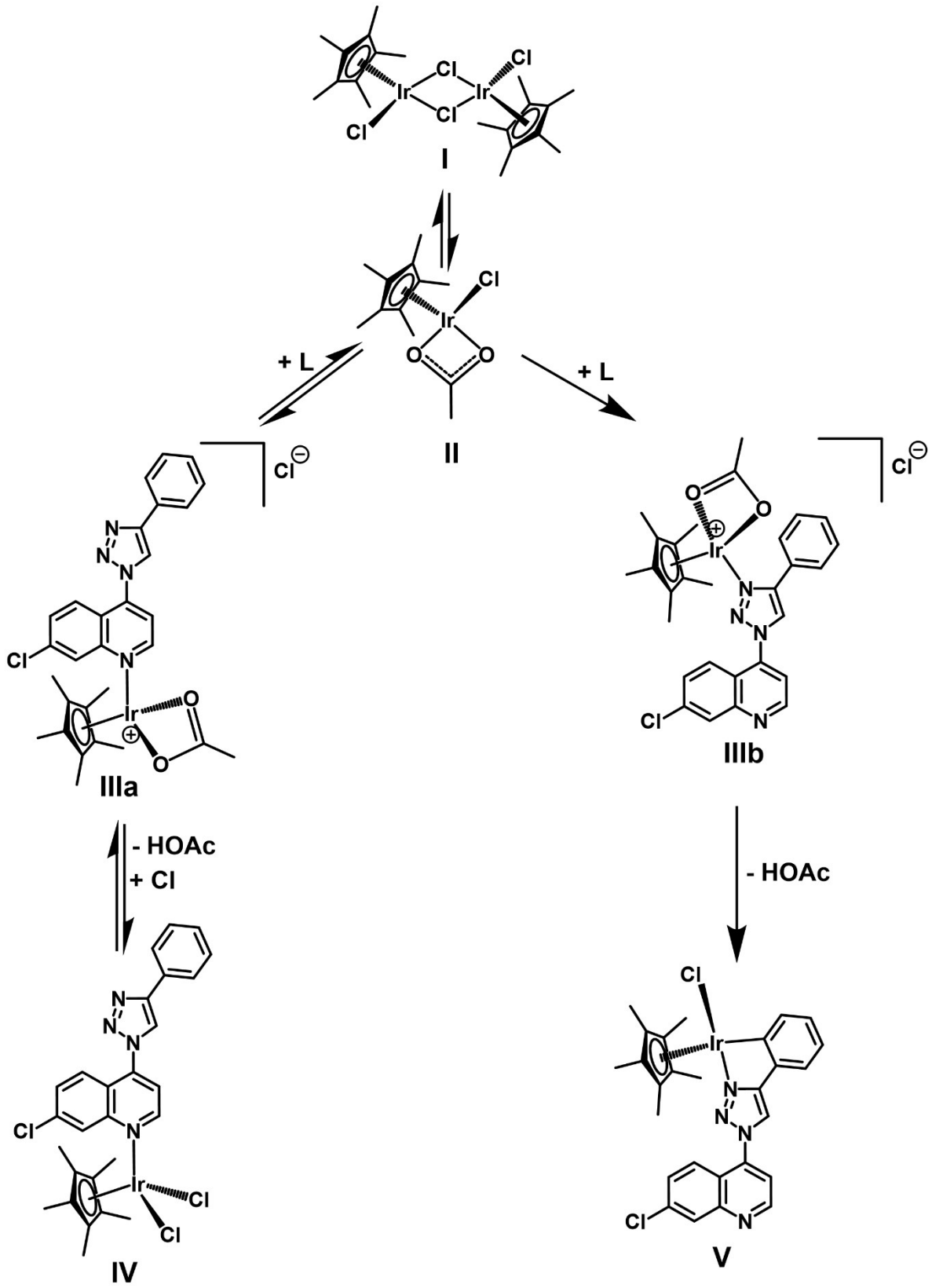

Fig. S29 Labelled pathway for the reaction process from the Ir Cp* dimer to the final complexes.

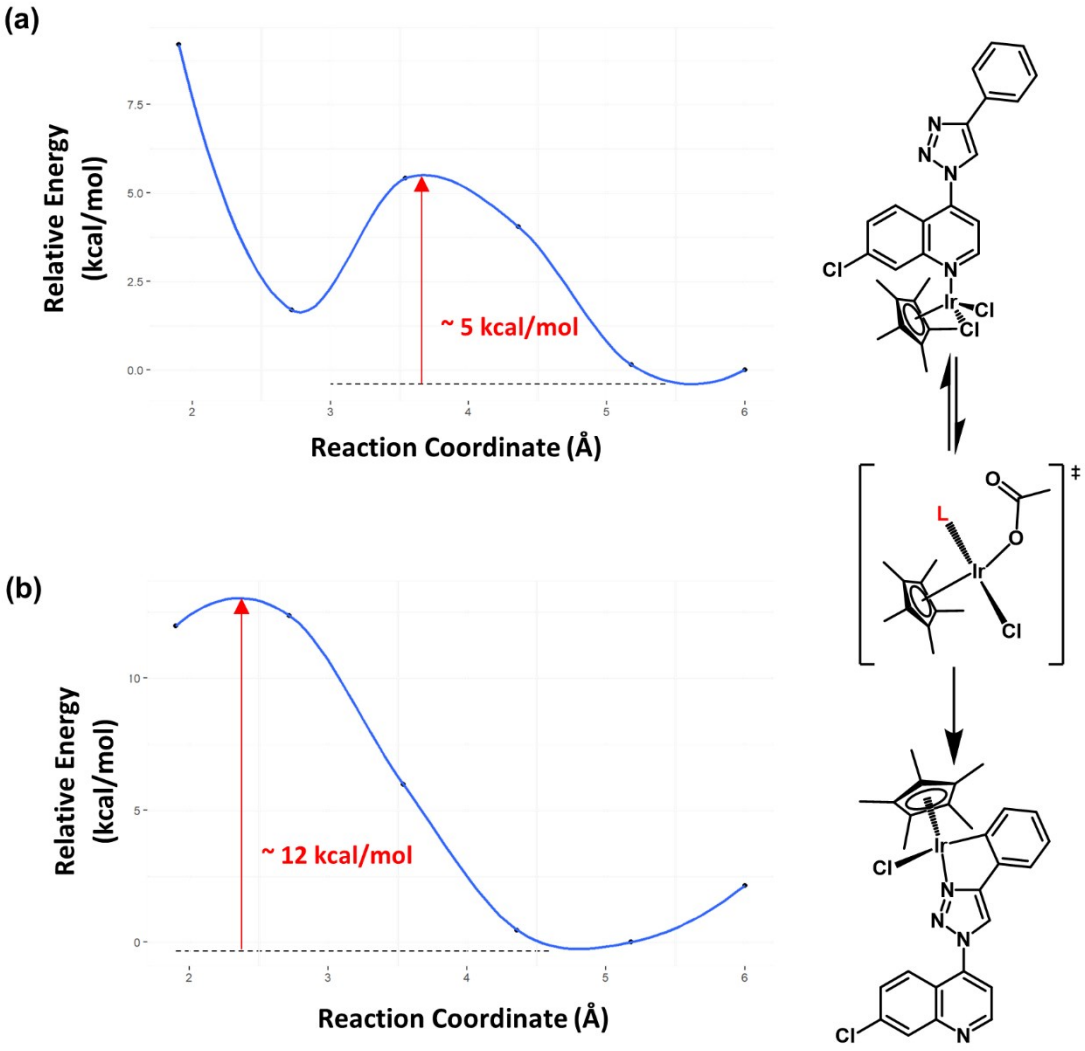

Fig. S30 Reverse energy diagrams of the two outcomes of metal coordination to the ligand at either (a) the quinoline nitrogen or (b) the triazole nitrogen.